Basin Research

IAS EAGE

Basin Research (2014) **26**, 403–435, doi: 10.1111/bre.12032

Crustal-scale fluid flow during the tectonic evolution of the Bighorn Basin (Wyoming, USA)

Nicolas Beaudoin,*,† Nicolas Bellahsen,*,† Olivier Lacombe,*,† Laurent Emmanuel*,† and Jacques Pironon‡

**UPMC Univ Paris 06, UMR 7193, ISTEP, F-75005, Paris, France*
†CNRS, UMR 7193, ISTEP, F-75005, Paris, France
‡Université, de Loraine, CNRS, CREGU, UMR 7359 Geo Resources, BP 70239, F-54506 Vandoeuvre-lés, Nancy Cedex, France

ABSTRACT

Stable isotope measurements (O, C, Sr), microthermometry and salinity measurements of fluid inclusions from different fracture populations in several anticlines of the Sevier-Laramide Bighorn basin (Wyoming, USA) were used to unravel the palaeohydrological evolution. New data on the microstructural setting were used to complement previous studies and refine the fracture sequence at basin scale. The latter provides the framework and timing of fluid migration events across the basin during the Sevier and Laramide orogenic phases. Since the Sevier tectonic loading of the foreland basin until its later involvement into the Laramide thick-skinned orogeny, three main fracture sets (out of seven) were found to have efficiently enhanced the hydraulic permeability of the sedimentary cover rocks. These pulses of fluid are attested by calcite crystals precipitated in veins from hydrothermal ($T > 120$ °C) radiogenic fluids derived from Cretaceous meteoric fluids that interacted with the Precambrian basement rocks. Between these events, vein calcite precipitated from formational fluids at chemical and thermal equilibrium with surrounding environment. At basin scale, the earliest hydrothermal pulse is documented in the western part of the basin during forebulge flexuring and the second one is documented in basement-cored folds during folding. In addition to this East/West diachronic opening of the cover rocks to hydrothermal pulses probably controlled by the tectonic style, a decrease in $^{87/86}$Sr values from West to East suggests a crustal-scale partially squeegee-type eastward fluid migration in both basement and cover rocks since the early phase of the Sevier contraction. The interpretation of palaeofluid system at basin scale also implies that joints developed under an extensional stress regime are better vertical drains than joints developed under strike-slip regime and enabled migration of basement-derived hydrothermal fluids.

INTRODUCTION

Foreland basins are often the location of multiple fluid flow events that have significant impacts on the chemical evolution of rocks, on the development of secondary porosity during diagenesis in carbonate rocks (e.g. Qing & Mountjoy, 1992; Bjørlykke, 1993, 1994; Roure *et al.*, 2005; Katz *et al.*, 2006; Vandeginste *et al.*, 2012) and on fracture development (Hubbert & Willis, 1957; Rubey & Hubbert, 1959; Templeton *et al.*, 1995; Billi, 2005). Major issues have been the understanding of the origin, pathways and interactions with rocks of fluids migrating in basins (Engelder, 1984; Reynolds & Lister, 1987; McCaig, 1988; Forster & Evans, 1991; Travé *et al.*, 2000, 2007; van Geet *et al.*, 2002; Ferket *et al.*, 2003; Roure *et al.*, 2005, 2010; Vilasi *et al.*, 2009; Bjørlykke, 2010; Evans, 2010; Li *et al.*, 2011), large-scale faults being efficient drains or barriers (Sibson, 1981). More recently, the distribution and development of fracture populations at fold scale appeared to influence local-scale hydrological systems, upon conditions of good connectivity and/or notable vertical persistence (e.g. Laubach *et al.*, 2009; Barbier *et al.*, 2012a). Rubey & Hubbert (1959) showed that the presence of fluids could facilitate faulting, and some authors invoked fluids to explain anomalous fault kinematics (e.g. Templeton *et al.*, 1995). Evans & Fischer (2012) highlighted the dynamic evolution of fluid system affecting strata during folding, and recent studies also suggest that structural style of deformation could influence palaeohydrology in fold-related fractures: in thin-skinned tectonics, fluids generally migrate in the décollement levels (when activated) and remain mainly stratified above the thrust tip until development of syn-folding fracture sets (e.g. Travé *et al.*, 2007; Fischer *et al.*, 2009; Dewever *et al.*, 2011; Evans *et al.*, 2012). In thick-skinned tectonics, the palaeohydrological systems

Correspondence: N. Beaudoin, UPMC Univ Paris 06, UMR 7193, ISTEP, F-75005, Paris, France. E-mail: nicolas.beaudoin@upmc.fr

are closed until basement thrusts are activated (McCaig, 1988), allowing for hydrothermal fluids to migrate in the overlying folded strata (Machel & Cavel, 1999; Katz *et al.*, 2006) where they could be efficiently drained by syn-folding fractures (Wiltschko *et al.*, 2009; Amrouch *et al.*, 2011; Beaudoin *et al.*, 2011). These fluid systems can be differentiated mainly by the nature of fluids that flow in strata during folding. Thus, one can wonder if the control of the structural style on the fluid system (i.e. origin and pathway) can be characterized during every stage of the development of folds and foreland basins (including stages of layer-parallel shortening and of late fold tightening).

The BigHorn Basin (BHB; Wyoming, USA), a (flexural) foreland basin in the frontal domain of the Laramide Rocky Mountains, shows several well-exposed folded structures (Fig. 1). There, the folded strata exhibit several fracture sets developed mainly during the Sevier and the Laramide orogenic events. A complex hydrological system is currently exploited in the basin, involving hydrothermal fluid resurgence zones seemingly linked to thick-skinned structures (Heasler & Hinckley, 1985). Thus, in this natural laboratory, a main issue is the influence of the development of the fracture pattern on the palaeohydrological system during the flexural evolution of the basin and its subsequent deformation during continuing thin- and thick-skinned deformational events, Sevier and Laramide, respectively. Key questions to be addressed are: What is the timing of fluid migration events in relation to fracture development? Did the fluid migration events record the switch from one tectonic style to the other, and thus, is there any notable influence of the structural style on the hydrological system? Is there a change in the origin of fluids during the basin evolution? What are the possible migration pathways in these different tectonic settings? In turn, can we recognize a possible role of fluid migrations on the microstructural evolution at the scale of the folded structure as well as at the scale of the entire basin?

For this purpose, fracture populations were documented throughout the basin, in four Laramide basement-cored structures: i.e. the Elk Basin anticline (EB; McCabe, 1948; Engelder *et al.*, 1997), the Little Sheep Mountain Anticline (LSMA), the Bighorn Mountains (BHM; Darton, 1905; Brown, 1988), and the Paintrock Anticline (PA; Stone, 2003) (Fig. 1a). To capture the first-order fracture pattern and sequence relevant for a palaeohydrological study at the basin scale, these new

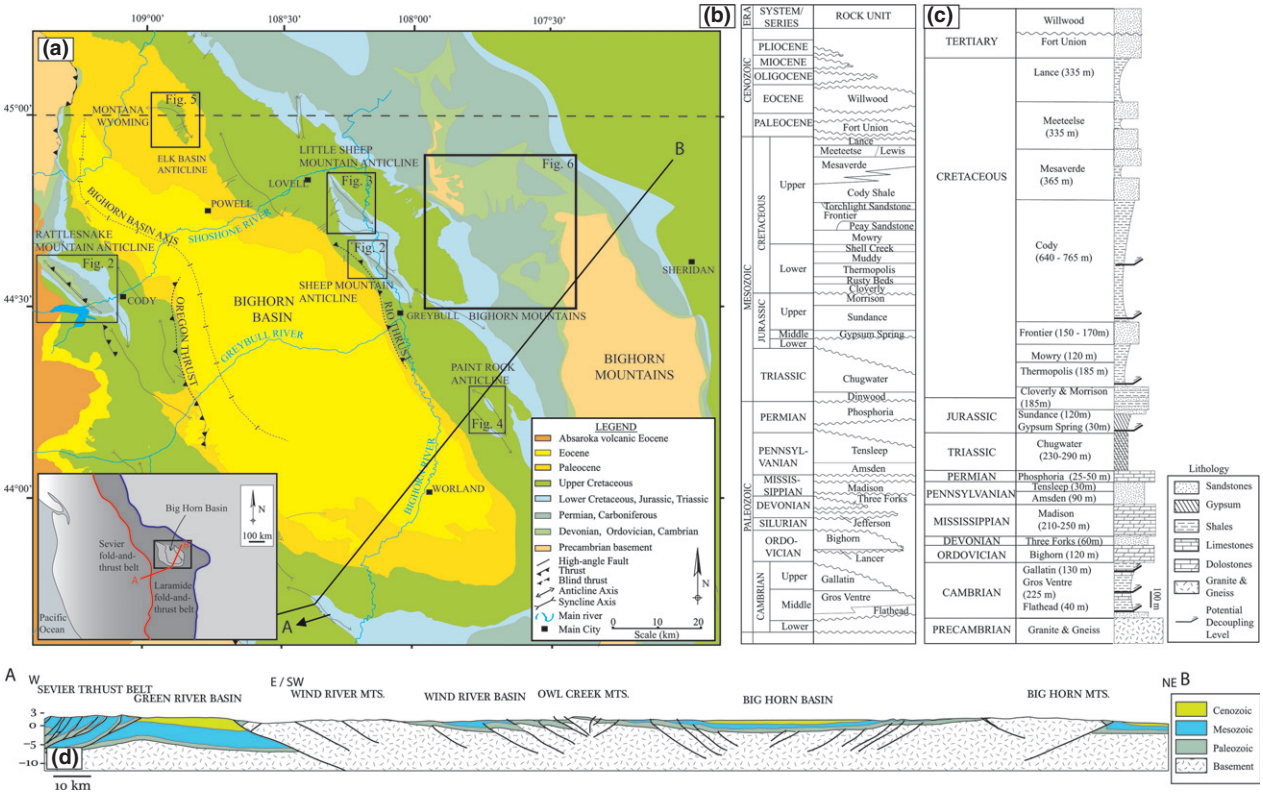

Fig. 1. (a) Geological map of the Bighorn Basin (Wyoming, USA, modified after Darton, 1905; Andrews et al., 1947), black boxes represent location of studied structures and related maps in Figs 2–6. The inset represents a map of the western portion of the North American craton, showing the Sevier and Laramide orogenic provinces, along with their respective present-day morphological fronts. Cross-section is reported as A-B. (b) Stratigraphic column of the Bighorn Basin, from west to east (modified after Fox & Dolton, 1995). (c) Synthetic stratigraphic column of the western Bighorn basin, modified after Durdella (2001) and Neely & Erslev (2009); potential decoupling levels are reported as thick black lines with arrows. (d) NE–SW cross-section across the Sevier belt and the Laramide belt, including the Bighorn Basin and the Bighorn Mountains (modified after Love & Christiansen, 1985; Stone, 1987).

investigations are combined with results previously obtained at Sheep Mountain Anticline (SMA; Bellahsen *et al.*, 2006a; Amrouch *et al.*, 2010) and at Rattlesnake Mountain Anticline (RMA; Beaudoin *et al.*, 2012). First, petrological and geochemical (oxygen, carbon and strontium isotope composition) analyses of calcite veins and of their host sedimentary rocks were performed along with fluid inclusion microthermometry and RAMAN microspectrometry to constrain the palaeohydrological systems at the fold scale. Second, the palaeohydrological evolution of the entire basin during its late Cretaceous–early Tertiary tectonic evolution was reconstructed based on each of the individual fluid systems, including the one previously reconstructed at SMA (Beaudoin *et al.*, 2011).

GEOLOGICAL SETTING

Bighorn Basin

The BHB is located in northwestern Wyoming, in the Laramide foreland province (Fig. 1a). The BHB was a portion of the Western Interior Basin during the thin-skinned Sevier orogeny (from late Jurassic), and a succession of shales and marls deposited. The flexural deformation included the basin since the Cenomanian, (Decelles, 2004), affecting the sedimentary column from Cambrian to Cretaceous (Fig. 1c; see Thomas, 1965; Fanshawe, 1971; Fox & Dolton, 1995). During Turonian times, the forebulge was back-driven in the western part of the BHB (Decelles, 2004), limiting the deposits in its western part. After that, thick shales were deposited in the BHB until the end of the Sevier orogeny. Then, this basin has been filled up during the thick-skinned Laramide orogeny (since Campanian, Fanshawe, 1971; Decelles, 1994, 2004; Fox & Dolton, 1995) as it got isolated and underwent endorheic evolution since the late Cretaceous (Fanshawe, 1971; Decelles, 2004), until the Eocene (Anderson & Picard, 1974) in response to the uplift of major basement arches (Blackstone, 1990), such as the BHM in the East (Crowley *et al.*, 2002). The Laramide contractional event probably reactivated pre-existing basement heterogeneities, such as Palaeozoic faults (Marshak *et al.*, 2000) or dykes (Erslev & Koenig, 2009), leading to the formation of the so-called Laramide uplifts, including mainly basement-cored folds of different wavelengths and amplitudes. Timing of eastward propagation of these Laramide uplifts is dated from Santonian/Campanian to Eocene times (25–30 Myr, Decelles, 2004 and references herein). Two major thrusts developed on each side of the BHB basin, the Oregon thrust to the west and the Rio thrust to the east (Brown, 1988; Stone, 1993; Fig. 1a), on which thick-skinned deformations are soled. The basement top shows little or no deformation in the centre of the basin (Fig. 1d). In the BHB, the Laramide-related Palaeocene depocentre was located east to the Oregon thrust (Thomas, 1965; Decelles, 2004) associated with a maximum of flexure in this (western) part of the basin.

Structure of studied folds

The RMA is a NW–SE striking, asymmetrical basement-cored fold located in the western part of the BHB (Fig. 2a, c; Stearns, 1978; Brown, 1988). RMA is 27 km long and 18 km wide. The 4-km thick sedimentary cover (from Cambrian to Upper Cretaceous) and the underlying basement were shortened during the Laramide compression. At RMA, the Precambrian basement rocks are exposed, overlain by Cambrian sandstones of the Flathead and the Gallatin Formations separated by the shaly Gros Ventre Formation (Fig. 1c). Those formations are overlain by the Ordovician dolostones of the Bighorn Formation, the Devonian sandstones of the Three Forks Formation, the Mississippian limestones/dolostones of the Madison Formation, the Mississippian shales and sandstones of the Amsden Formation, the Pennsylvanian sandstones of the Tensleep Formation and the Permian limestones of the Phosphoria Formation (Fig. 1c).

The SMA and the LSMA are NW–SE striking asymmetrical anticlines located in the eastern part of the basin (Figs 1a, 2b and 3) where formations from Mississippian to Cretaceous are exposed. SMA is 17 km long and 5 km wide (Fig. 2b), while LSMA is 14 km long and 10 km wide (Fig. 3). The Laramide compression affected the 3.2 km thick sedimentary cover (from basement rocks to the upper Cretaceous ones). At LSMA and SMA, the oldest rocks cropping out are the Mississippian limestones of the Madison Formation, overlain by the Mississippian and Pennsylvanian sandstones of the Amsden and Tensleep Formations. Above are the Permian limestones of the Phosphoria Formation and the Triassic gypsum and shales of the Chugwater Formation. SMA is interpreted as a basement-cored fold (Fig. 2d; Hennier & Spang, 1983; Forster *et al.*, 1996; Savage & Cooke, 2004; Stanton & Erslev, 2004; Stone, 2004; Bellahsen *et al.*, 2006b; Fiore Allwardt *et al.*, 2007; Amrouch *et al.*, 2010), and given the similarity and the vicinity of LSMA, this structure can also be reliably considered as basement-cored.

The PA located near the Bonanza oilfield (BO), to the southeast of the BHB, strikes NW–SE and is 10 km long and 4 km wide (Fig. 4). In spite of being of shorter amplitude and wavelength than other folds from the BHB, PA is interpreted as a basement-cored anticline (Stone, 1987, 2003). The Jurassic sandstones/limestones of the Sundance Formation and the Jurassic to Cretaceous shales and sandstones of the Cloverly and Morrison Formation crop out; the Lower Cretaceous shales of the Thermopolis Formation overlie them.

The EB is located in the northern part of the BHB, at the Montana-Wyoming state border (Fig. 1a). EB is a breached anticline related to the Elk basin basement thrust (Stone, 1993; Engelder *et al.*, 1997). This curved anticline strikes from NNW–SSE to WNW–ESE from South to North and is 12 km long and 7 km wide

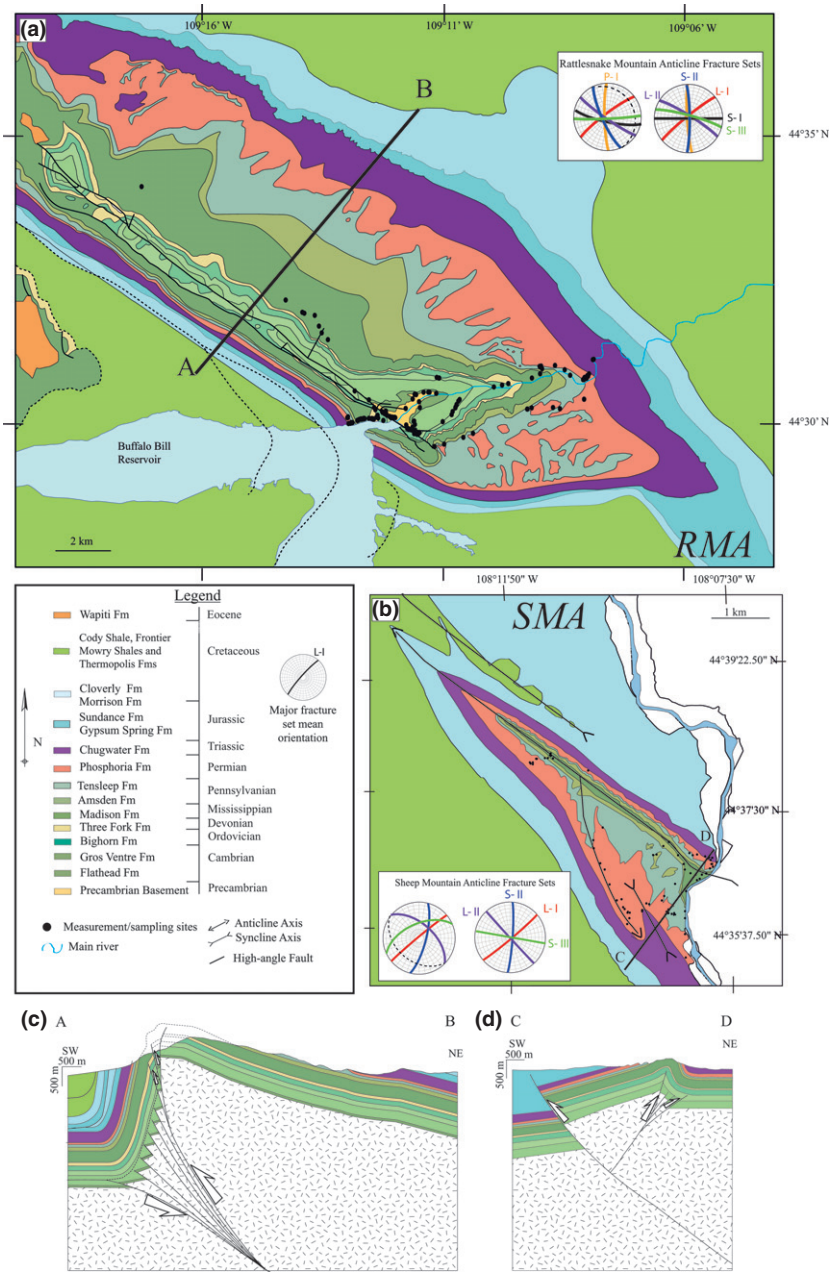

Fig. 2. (a) Simplified geological map of the Rattlesnake Mountain Anticline (after Pierce, 1966; Pierce & Nelson, 1968). (b) Simplified geological map of the Sheep Mountain Anticline (after Rioux, 1994). Dots represent measurement sites and sampling locations. Thick lines represent the cross-section lines. The corresponding fracture sets are represented on stereodiagrams (Schmidt lower hemisphere, equal area stereonets) in the strata current attitude (left diagram) and after unfolding (right diagram) in the respective backlimb of folds (Bellahsen *et al.*, 2006a; Amrouch *et al.*, 2010; Beaudoin *et al.*, 2012). On stereoplots, the black line represents the mean plane of set S-I, the blue line set S-II, the green line set S-III, the red line set L-I, the purple line set L-II and the orange line set P-I. (c) Cross-section of Rattlesnake Mountain Anticline (after Beaudoin *et al.*, 2012). (d) Cross-section of Sheep Mountain Anticline (after Amrouch *et al.*, 2010; Beaudoin *et al.*, 2011).

(Fig. 5a). In the EB, the sedimentary cover is nearly preserved, and offers outcrops of Upper Cretaceous to Palaeocene rocks (Fig. 5a). It comprises the Campanian Cody shale Formation, the Campanian shales and sandstones of the Eagle, Claggett Shale, Judith River and Bearpaw Formations (formally equivalent to the Mesaverde and Meeteeste Formations in Wyoming), the Maastrichtian sandstones of the Lance Fm., and the Palaeocene sandstones of the Fort Union Formation.

The BHM compose the major basement arch of the BHB (Fig. 1a; Brown, 1988). This asymmetrical basement-cored fold, striking NNW–SSE, is 140 km long and 100 km wide. The basement rocks crop out in a large part of the BHM and the remains of the sedimentary

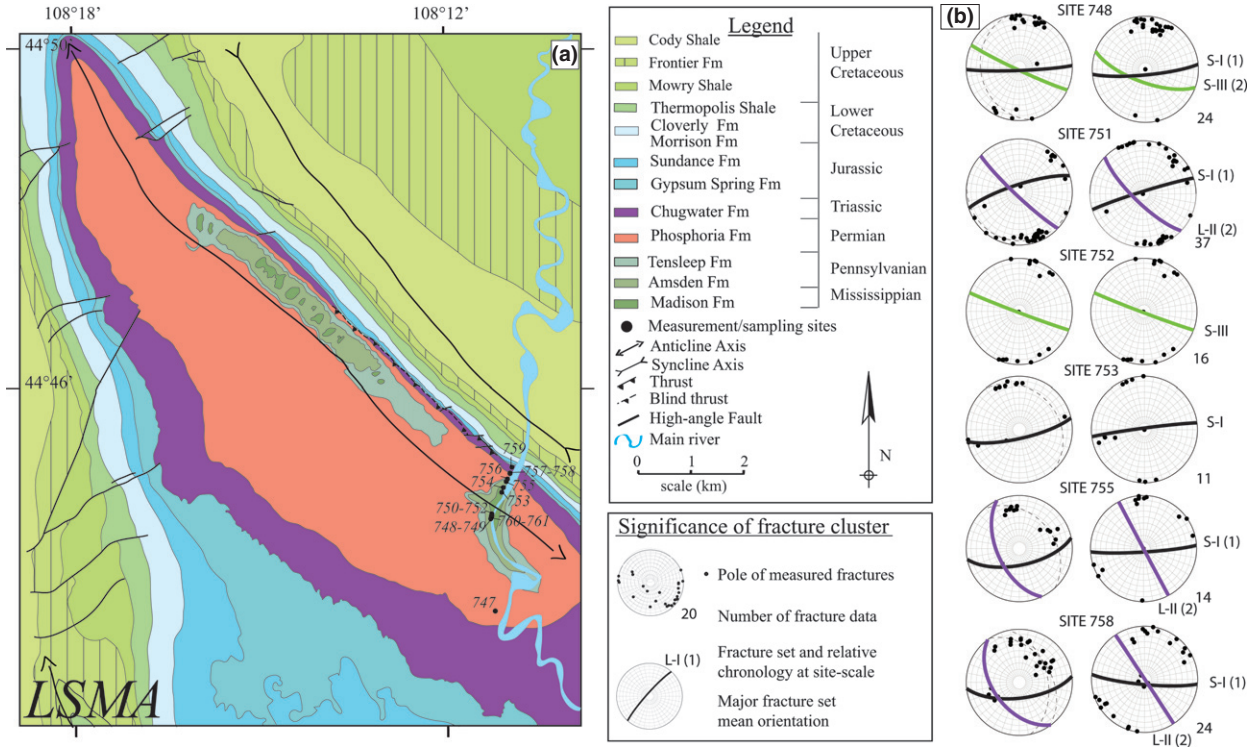

Fig. 3. (a) Simplified geological map of Little Sheep Mountain Anticline (after Rioux, 1994). Dots represent measurement sites and sampling locations. (b) Results of fracture analysis for each site, including raw data (poles to fractures) and main fracture set orientations, in the strata current attitude (left diagram) and after unfolding (right diagram) (Schmidt's lower hemisphere, equal area stereonets). Same key as in Fig. 2.

cover are located in the backlimb of the BHM. Thus, the main study area of the BHM is located in the eastern part of this limb (Figs 1a and 6a) where the 3-km thick cover presents the same formations and lithologies as those exposed at RMA.

Microstructural setting

Fracture populations and their sequential development through time were previously defined at SMA (Bellahsen *et al.*, 2006a; Amrouch *et al.*, 2010) and at RMA (Beaudoin *et al.*, 2012). These sequences include several successive fracture sets. Different names have been used in previous studies; we will use hereinafter the one used in Beaudoin *et al.* (2012).

The oldest fracture set (set S-I) is composed of joints/veins striking mainly E–W, which is related to an early Sevier phase of Layer-Parallel Shortening (LPS) that affected the western part of the BHB (Beaudoin *et al.*, 2012; Weil & Yonkee, 2012). A second set of joints/veins striking mainly N–S (set S-II) has been tentatively related to the late Cretaceous flexural evolution of the basin. This set has been widely recognized at RMA (Beaudoin *et al.*, 2012), but poorly observed at SMA (Amrouch *et al.*, 2010). A third set of joints and veins that strikes 110° E (set S-III), later reactivated by left-lateral shearing, has been described in both SMA and RMA, and has been related to a late stage of the Sevier LPS (Amrouch *et al.*, 2010). This last set appears to be stratabound in SMA, whereas it displays a much higher vertical persistence at RMA (Barbier *et al.*, 2012a, b).

The Laramide-related fractures comprise three sets: the first set is composed of bed-perpendicular joints and veins striking NE–SW (Set L-I), related to the LPS phase of the Laramide event during which reverse faults also developed (Bellahsen *et al.*, 2006a, b; Amrouch *et al.*, 2010; Weil & Yonkee, 2012). The second Laramide-related set (set L-II) is made of joints and veins that strike parallel to fold axes (*ca.* 130° E), being mainly located at their hinges. This set appears to have a high vertical persistence at SMA (Beaudoin *et al.*, 2011; Barbier *et al.*, 2012a, b) and is interpreted as related to layer curvature during folding. A third fracture set (set L-III) comprises small-scale newly formed strike-faults and reverse faults and reactivated joints/veins witnessing a NE–SW-directed compression during a late stage fold tightening in both folds (Amrouch *et al.*, 2010; Beaudoin *et al.*, 2012).

Finally, a set of joints and veins striking N–S and highly vertically persistent has been described exclusively at RMA (set P-I), probably related to a post-Laramide extensional event (Eocene Core Complexes or Miocene Basin-and-Range extension) that occurred west of the basin, and affected only its western part (Beaudoin *et al.*, 2012).

Engelder *et al.* (1997) defined two different joint sets at EB, with a sequence relative to the structural develop-

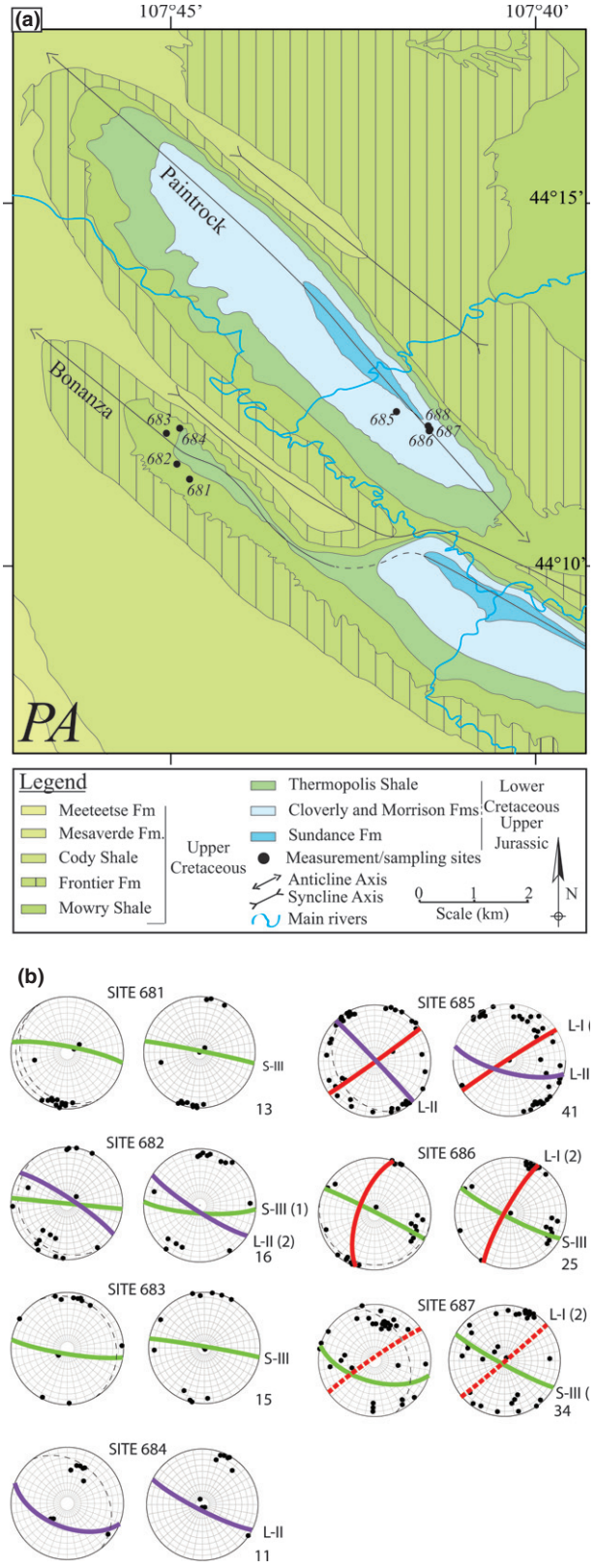

Fig. 4. (a) Simplified geological map of the Bonanza oilfield and Paintrock Anticline (after Rogers et al., 1948). Dots represent measurement sites and sampling locations. (b) Results of fracture analysis for each site (same key as in Fig. 2). The dashed line highlights a fracture set that is poorly encountered at the scale of the site, but well represented at the fold scale.

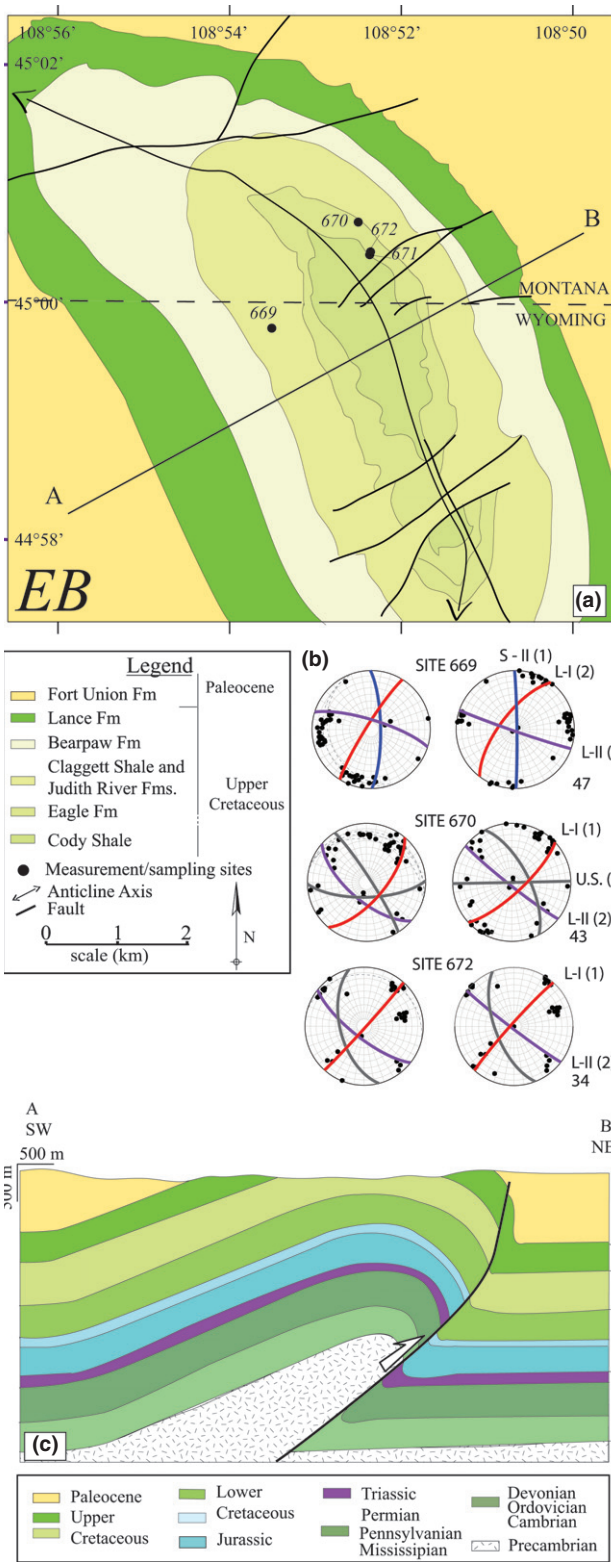

Fig. 5. (a) Simplified geological map of the Elk Basin Anticline (modified after Engelder et al., 1997; Lopez, 2000). Dots represent measurement sites and sampling locations. (b) Results of fracture analysis for each site (same key as in Fig. 2) Fracture sets symbolized with a grey line were documented at only one measurement site and, as a consequence, were not integrated in the fracturing sequence at fold-scale. (c) Cross-section of Elk Basin Anticline (Engelder et al., 1997) based on a time-migrated, interpreted seismic profile from Stone (1993).

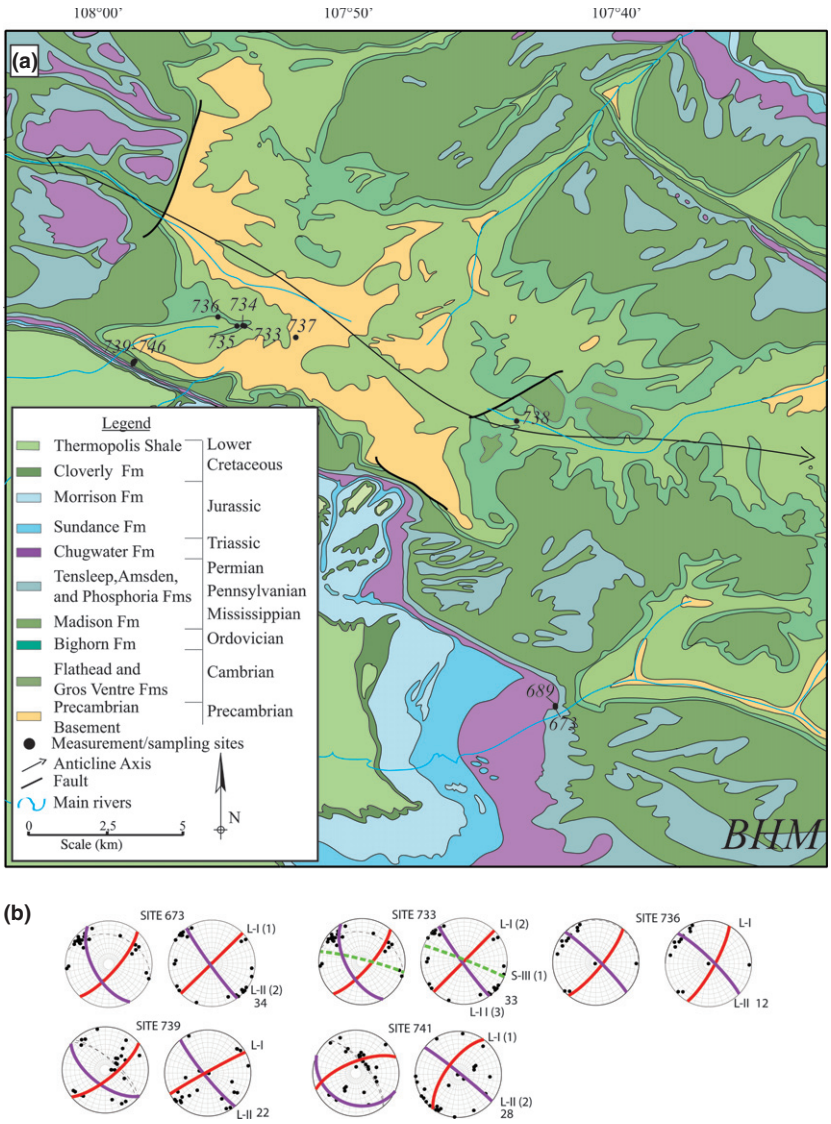

Fig. 6. (a) Simplified geological map of the western portion of the Bighorn Mountains (after Darton, 1905). Dots represent measurement sites and sampling locations. (b) Results of fracture analysis for each site, same key as in Fig. 2.

ment of the curved anticline, with a first joint set striking perpendicular to the fold (mainly ENE–WSW) and a second joint set striking parallel to the fold axis (from NW–SE to WNW–ESE). Nevertheless, these authors highlighted that NE–SW trending joints were poorly developed at EB.

ANALYTICAL METHODS

Sampling

At RMA, sampling for geochemical analysis covered every fracture set, in all exposed formations, and in all accessible structural positions. Most samples were collected within the Shoshone canyon and are located along two cross-sections (Fig. 2a). The other folds were sampled regarding fractures and lithologies, with priority to the well-mineralized Laramide-related fractures. At LSMA, sampling was performed in all formations and all fracture sets along the Bighorn river (Fig. 3a). In PA, because of the poor quality of outcrops, sampling was restricted to the southern termination of the fold (Fig. 4a). In EB, no sample was taken for geochemical analysis due to the lack of mineralized fractures. Fracture-measurement sites are located along a cross-section striking perpendicular to the fold axis in its northern part (Fig. 5a). In BHM, sampling was carried out in the backlimb of the arch where cover rocks crop out (Fig. 6a).

Fracture analysis

Nearly 600 fracture orientation data were collected in 28 sites on LSMA, BHM, EB and PA in both the sedimentary cover and the basement (at BHM) (Table 1) to complement and to expand previous fracture studies in SMA (Bellahsen *et al.*, 2006a) and RMA (Beaudoin *et al.*, 2012). The comparison of these fold-related fracture populations with the previously defined fracture sequence in

Table 1. Characteristics of sites of fracture measurements and vein sampling

Structure	Site	Latitude	Longitude	Formation
Elk Basin Anticline	669	108°53′25.26″ W	44°59′46.45″ N	Claggett Shale
	670	108°52′23.72″ W	45°0′39.94″ N	Eagle
	671	108°52′15.56″ W	45°0′23.49″ N	Cody Shale
	672	108°52′14.96″ W	45°0′24.94″ N	Cody Shale
Paintrock Anticline	681	107°44′44.56″ W	44°11′12.79″ N	Mowry Shale
	682	107°44′55.00″ W	44°11′25.24″ N	Mowry Shale
	683	107°45′3.60″ W	44°11′50.58″ N	Mowry Shale
	684	107°44′52.63″ W	44°11′54.73″ N	Mowry Shale
	685	107°41′54.46″ W	44°12′8.40″ N	Cloverly and Morrison
	686	107°41′27.52″ W	44°11′52.62″ N	Cloverly and Morrison
	687	107°41′26.82″ W	44°11′53.90″ N	Cloverly and Morrison
	688	107°41′28.40″ W	44°11′56.67″ N	Cloverly and Morrison
Bighorn Mountains	673	107°42′0.62″ W	44°34′27.07″ N	Phosphoria
	689	107°42′0.35″ W	44°34′29.60″ N	Phosphoria
	733	107°53′51.51″ W	44°49′3.06″ N	Bighorn
	734	107°53′55.81″ W	44°49′4.04″ N	Bighorn
	735	107°54′9.34″ W	44°49′3.09″ N	Bighorn
	736	107°54′52.83″ W	44°49′24.05″ N	Bighorn
	737	107°51′54.71″ W	44°48′36.97″ N	Basement
	738	107°43′29.16″ W	44°45′25.10″ N	Gros Ventre
	739	107°58′3.30″ W	44°47′42.54″ N	Madison
	740	107°58′3.93″ W	44°47′41.99″ N	Madison
	741	107°58′4.38″ W	44°47′41.93″ N	Madison
	742	107°58′5.30″ W	44°47′41.25″ N	Madison
	743	107°58′5.39″ W	44°47’ 41.31″ N	Madison
	744	107°58′6.57″ W	44°47’ 40.03″ N	Madison
	745	107°58′7.20″ W	44°47′39.17″ N	Phosphoria
	746	107°58′7.27″ W	44°47′36.49″ N	Phosphoria
Little Sheep Mountain Anticline	747	108°11′23.77″ W	44°43′43.89″ N	Phosphoria
	748	108°11′28.06″ W	44°44′45.11″ N	Amsden
	749	108°11′28.07″ W	44°44′45.19″ N	Amsden
	750	108°11′26.99″ W	44°44′47.11″ N	Madison
	751	108°11′27.34″ W	44°44′47.23″ N	Madison
	752	108°11′27.03″ W	44°44′48.38″ N	Madison
	753	108°11′17.81″ W	44°45′2.70″ N	Madison
	754	108°11′16.29″ W	44°45′5.84″ N	Madison
	755	108°11′13.61″ W	44°45′9.81″ N	Amsden
	756	108°11′12.38″ W	44°45′11.49″ N	Tensleep
	757	108°11′10.06″ W	44°45′15.17″ N	Phosphoria
	758	108°11′9.97″ W	44°45′15.57″ N	Phosphoria
	759	108°11′8.24″ W	44°45′19.39″ N	Gypsum Spring
	760	108°11′27.19″ W	44°44′46.41″ N	Madison
	761	108°11′27.64″ W	44°44′46.18″ N	Madison

SMA and RMA constrains the fracture pattern relevant at basin scale. Fracture sets were independently defined for each site on the basis of common orientation (strike and dip after unfolding or in their current attitude) and mode of deformation (opening or shearing) defined in the field and in thin-sections (cut perpendicular to mineralized vein strike). Mode I opening is supported either by the lack of positive evidence of shearing and grain crushing along vein boundaries or by direct observations, such as offsets of clasts (Fig. 7a) and/or by the pattern of crystal growth within the veins. Fractures clearly opened in mode I will be named joints when empty and veins when mineralized in accordance with their common opening mode (Engelder, 1987). Fractures with ambiguous deformation mode will simply be named fractures hereinafter and will not be used in our interpretation.

The mean orientation of each fracture set was statistically computed using a software developed at IFPEN for the automatic definition of fracture clusters (see Bellahsen *et al.*, 2006a; Ahmadhadi *et al.*, 2008). The data are presented on stereonets of fracture orientation at each measurement site that are not weighted by abundance of fractures, as we believe that this parameter can be biased by outcrop conditions. However, we carefully observed the main characteristics of each fracture set (i.e. geometry of fracture planes, range of orientation within each set,

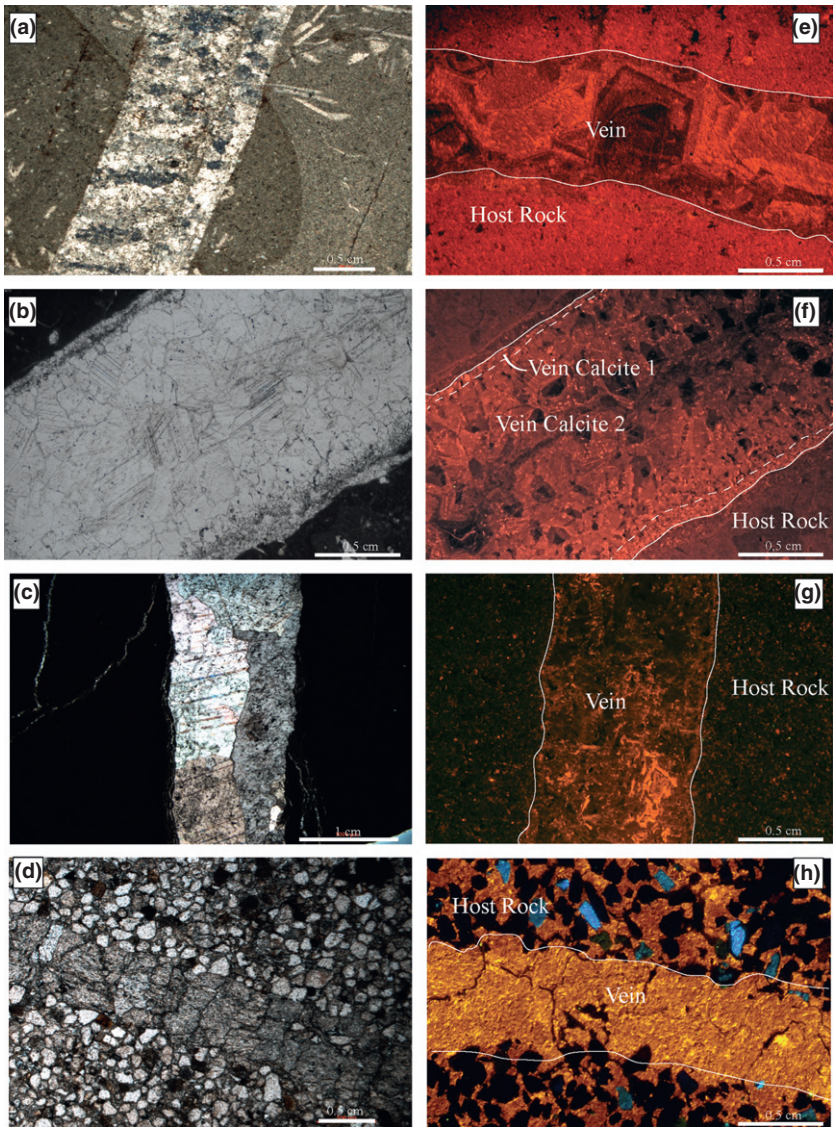

Fig. 7. Left column: Petrological observations of veins and host-rocks illustrating the opening mode of veins as supported by offset of elements of the host-rock (a: RMA), by the straight outline between vein and host-rock (b: BHM, c: LSMA), or by the presence of fibrous crystals (d: PA). Right column: cathodo luminescence observations of veins and host-rocks, exhibiting different patterns of luminescence: zoned luminescence (e: RMA, f: BM), heterogeneous luminescence (g: LSMA) and homogeneous luminescence (h: PA). White lines highlight boundaries between vein and host-rock and between different generations of cements in veins (f). Differences between red luminescence in the host-rock and orange luminescence in the matrix are illustrated on photomicrographs e, f and g, while h illustrates a common luminescence between vein calcite and carbonate portion of host-rock. Photomicrographs f, g and h correspond to photomicrographs b, c and d, respectively.

vertical extent and length), along with chronological relationships (Fig. 8) to establish a reliable fracture sequence.

Petrography and Mineralogy

Representative host-rocks and cements were analysed by X-ray powder diffraction on a SIEMENS D501 X-ray diffractometer (Fig. 9). To investigate the diagenetic state of both veins and host-rocks, petrographic observations were carried out on polished thin-sections of 30 μm thick under an optical microscope and under cathodoluminescence microscopy using a cathodoluminescence Cathodyne Opea device with a cold cathode system. Operating conditions were in the range of 200–400 μA and 13–18 kV gun current and at a constant 60 mTorr vacuum. The microstructural characteristics of veins, such as opening mode, veins/matrix geometrical relationships and vein cross-cutting relationships were determined under an optical microscope.

Geochemical characterization of palaeofluids

Oxygen and carbon stable isotope analysis

$\delta^{13}C$ and $\delta^{18}O$ analyses were performed on veins and host-rocks from RMA (67 samples), LSMA (10 samples), BHM (10 samples) and PA (3 samples) using an auto-

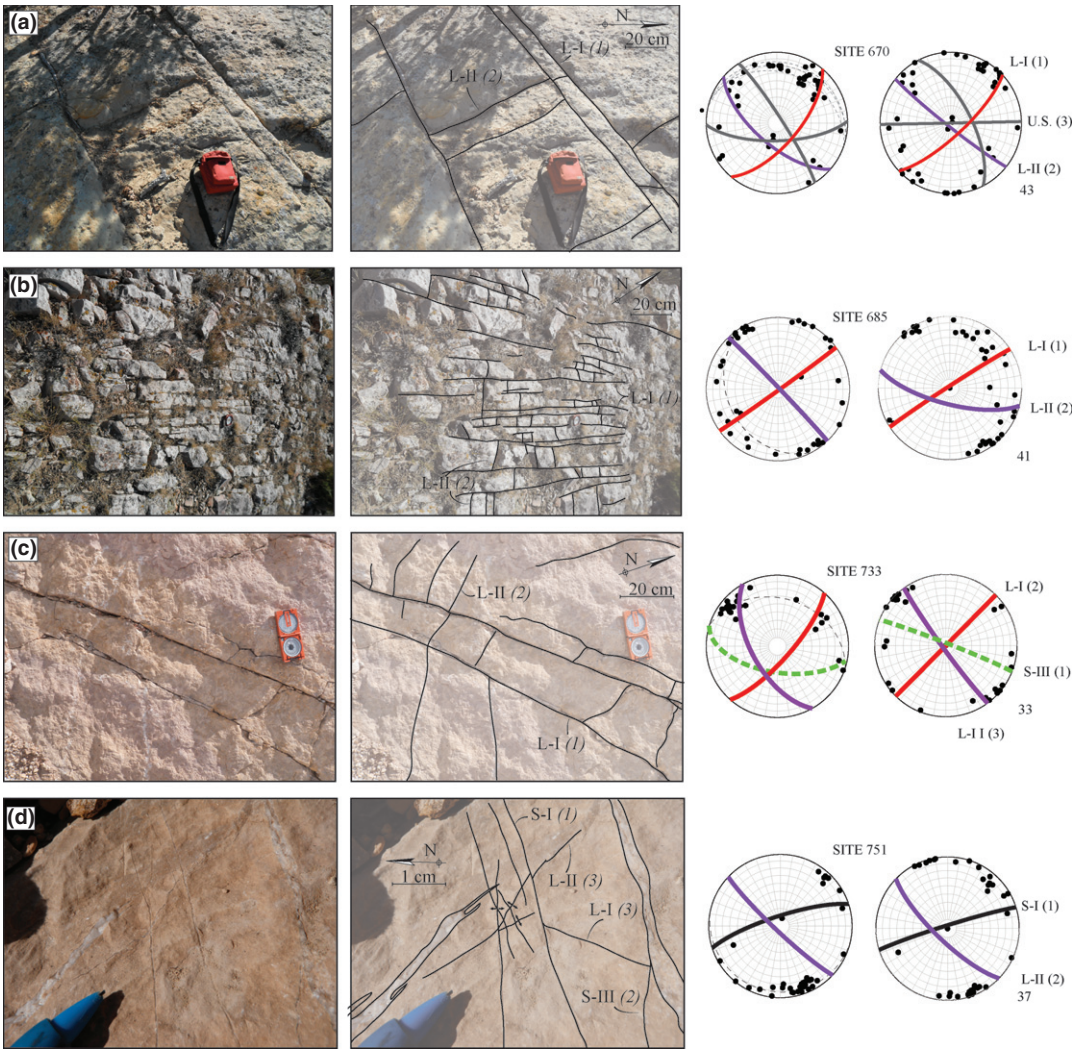

Fig. 8. Photographs and interpretations of fracture patterns along with chronological relationships at (a) Elk Basin, (b) Paintrock Anticline, (c) Bighorn Mountains, (d) Little Sheep Mountain Anticline. Next to each photograph are shown stereodiagrams (Schmidt's lower hemisphere) with statistically computed mean fracture planes defining the fracture sets in the current strata attitude (left) and after unfolding (right).

mated preparation device coupled to an Isoprime gas-ratio mass spectrometer to constrain the geochemical signature of calcite cements of veins, the origin of fluids from which those cements precipitated and the palaeo-fluid system evolution through space and time. Following the same protocol as the previously published work on SMA samples (reported on Fig. 10 after Beaudoin *et al.*, 2011), veins were hand-drilled or micro-milled to avoid mixture with host-rocks. Samples were placed in glass vials and reacted with dehydrated phosphoric acid under vacuum at 90 °C, requiring a correction for dolomite samples defined by Rosenbaum & Sheppard (1986). Hereinafter, all values for both veins and host-rocks are reported in permil (‰) relative to the Vienna Pee Dee Belemnite (VPDB or PDB) for carbon and for oxygen with an accuracy of 0.05‰ and 0.1‰ respectively (Table S1).

Strontium isotope analysis

$^{87}Sr/^{86}Sr$ isotope measurements were performed on fifteen samples representative of the Laramide-related veins in RMA (11 samples), LSMA (1 sample) and BHM (3 samples) to extend previously published work on SMA (9 samples reported on Fig. 11, Beaudoin *et al.*, 2011). $^{87}Sr/^{86}Sr$ isotope ratios were used to define the origin and migration pathways of palaeofluids by comparison of ratios obtained from veins (11 samples) with ratios obtained from the Precambrian granitic rocks (3 samples) and from limestones of the Ordovician Bighorn Formation (1 sample). The analyses were performed at the Geochronology and Isotopic Geochemistry Laboratory in the Universidad Complutense de Madrid. Two different dissolution routines were applied according to the cement mineralogy. Previously weighted samples of calcite in Teflon® vials

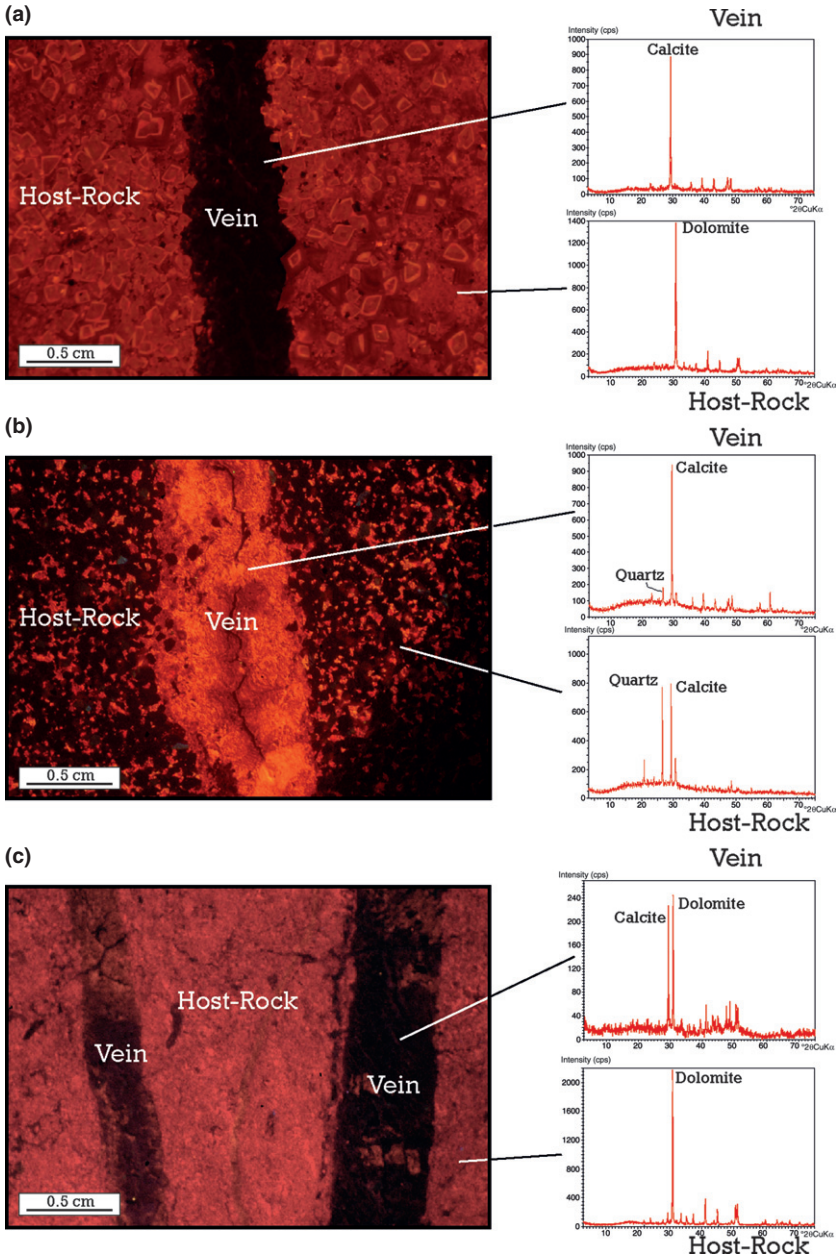

Fig. 9. Photomicrographs under cathodoluminescence and corresponding spectrographs obtained by X-ray diffractometry illustrating the type of veins used in the study (a, b) or rejected (c) for isotopic analyses. (a) sample BM14 (BHM, Madison Fm.) shows a single phase nonluminescent calcite vein in dolomitic host-rock. (b) sample 31T (SMA, Tensleep Fm.) shows a single phase orange bright luminescent calcite veins with growth rims in host-rock constituted by quartz and orange bright luminescent calcite. (c) sample 38–9 (SMA, Madison Fm) shows veins with both nonluminescent calcite and dull red luminescent dolomite in a dolomitic host-rock.

were dissolved in 3 ml of pure 2.5 M hydrochloric acid, over a period of 2 h at room temperature. Subsequently, samples were centrifuged at 2049 *g* during 10 min. Sr was separated from other elements using cation exchange chromatography with Dowex 50W-X12 resin. Sr samples were collected in clean vials and evaporated at 80 °C. Concerning granite samples, weighted in Teflon® vials, they were dissolved in a solution of 2 ml of nitric acid and 5 ml of fluoric acid during two days at 120 °C. After drying at 80 °C, 2 ml of nitric acid was added and the solution was dried again (80 °C). Residues were dissolved in 5 ml of dissolved hydrochloric acid (6 M) and put at 120 °C for 12 h. Dried samples were then dissolved in 3 ml of distilled 2.5 M chloryhydric acid and centrifuged at 4000 r.p.m. regardless of the mineralogy. Dry Sr samples were loaded along with 1 µl of phosphoric acid (1 M) over a single tantalum filament and were introduced into the Micromass VG Sector-54 Thermal Ionization Mass Spectrometer (TIMS) and analysed using a dynamic multicollection method (five Faraday detectors) with 150 scans.

Strontium results were corrected for ^{87}Rb interferences. The $^{87}Sr/^{86}Sr$ ratios were normalized using as reference the radiogenic stable ratio ($^{88}Sr/^{86}Sr$: 0.1194). This normalization corrects the mass fractionation in the sample

through the load and the total analysis time. SRM 987 was chosen as isotopic standard of Sr to be analysed at the same time with samples. Each sample was analysed eight times with an analytical error of the laboratory in the $^{87}Sr/^{86}Sr$ ratio of 0.01% (average values are reported in Table S1).

Microthermometric study of fluid inclusions

The microthermometric study of fluid inclusions was performed on quartz/calcite veins sampled in RMA, LSMA, BHM, SMA and PA to complement previous fluid inclusion studies performed at SMA (Katz *et al.*, 2006; Beaudoin *et al.*, 2011; Barbier *et al.*, 2012a, b) and at RMA (Katz *et al.*, 2006). 100 μm doubly polished thick sections were prepared and analysed on Linkam Pr 600 and on Linkam MD600 microthermometric stages. Sampling covered all limestone and sandstone formations, wherein respectively 36 and 47 nondeformed two-phase primary and pseudo-secondary fluid inclusions were identified in limestones and in sandstones, respectively, along with 25 nondeformed two-phase secondary fluid inclusions (Fig. 12). Primary and pseudo-secondary fluid inclusions seemingly have low vapour–liquid ratios, which are constant in the same assemblage (Fig. 12a). Observations under optical microscope were performed to control the diagenetic evolution of the crystal hosting the inclusions directly on the studied thick sections, while observations under cathodoluminescence microscopy were performed on mirror thin sections. Samples were heated at a rate of 15 °C per minute until the vapour bubble decreased in size; heating rate was slowed at less than 1 °C per minute to determine the homogenization temperature of the fluid inclusion. All measurements are reproducible with an accuracy of ±0.5 °C. To avoid decrepitation of fluid inclusion in calcite due to freezing, the salinity was checked using Raman microspectrometer by the method developed by Dubessy *et al.* (2002). The Raman microprobe is a Labram type (Horiba–Jobin–Yvon®) with Edge® filters, using a grating of 1800 grooves per mm. The detector is a CCD, cooled at the temperature of liquid nitrogen. The exciting radiation at 514 nm was provided by an Ar^+ laser (type 2020, Spectraphysics®). Spectral resolution is around 2 cm^{-1}. Raman was also used to detect the presence of dissolved water in liquid n-tetradecane. Salinity check was performed on both two-phase and single-phase fluid inclusions, with respect to their timing of development, in 18 and 24 fluid inclusions in limestones and sandstones respectively. Our data are presented in Table 1, as well as those previously published by Katz *et al.* (2006), Beaudoin *et al.* (2011) and Barbier *et al.* (2012a, b).

RESULTS

Fracture populations at fold-scale

Statistical analyses of fracture orientation combined with chronological relationships allow the definition of 6 different joint/vein sets in the four-folds (EB, PA, LSMA and BHM). Like in SMA and RMA, these fracture sets are composed of joints and veins, and sets S-I to L-II are made up with bed-perpendicular joints/veins.

Fracture population at LSMA was divided into 3 different sets including bed-perpendicular joints and veins (Fig. 3b). The oldest one is composed of veins and joints striking E-W after unfolding. This set was observed in all structural positions of the fold and in all sites. Two different sets, with no directly observed chronological relationship between them, abut on the E–W set: a set with joints and veins oriented 110° E, documented only in the backlimb (Fig. 3, sites 748, 752), and a set documented in both the forelimb and the backlimb (Fig. 3, sites 751, 755, 758) including joints and veins that strike NW–SE, parallel to the fold hinge (Fig. 8d). The relative chronology and the orientation of fractures are consistent throughout the different studied formations.

Three sets of bed-perpendicular joints and veins were defined at the BO and PA (Fig. 4). These joint sets comprise only joints at BO while they comprise both joints and veins at PA. The first set displays joints (and veins for PA) striking 110° E at BO (Fig. 4, sites 681, 682, 683) and 120° E at PA (Fig. 4, sites 686, 687) after unfolding. These are documented in both structures and predate all the other fracture sets, which have common orientations in both folds. The second fracture set comprises joints and veins oriented NE–SW that abut on the 120° E one and was documented in all sites at PA (Fig. 4, sites 685, 686, 687). A last set gathers joints and veins oriented NW–SE after unfolding that abuts on joints oriented 110° E and on veins and joints oriented NE–SW, respectively at BO (Fig. 4, site 682) and PA (Fig. 4, site 685; Fig. 8b). According to the low strata dip, it is difficult to check whether these last fractures developed before or after folding. However, because their strike is parallel to the local trend of the fold axis, they can reliably be considered as syn-folding fractures formed in response to local strata curvature at fold hinge.

The fracture population at EB exhibits 5 bed-perpendicular sets of joints: the oldest one was documented in the backlimb of the fold (Fig. 5, site 669), and strikes N–S after unfolding. A second set, documented at three sites, comprises joints striking NE–SW (045° E) after unfolding that abuts on joints oriented N–S (Fig. 5). Two sets of joints abut on this NE–SW set (Fig. 8a): one is found in the backlimb, with a 110° E trend after unfolding (Fig. 5, site 669) and a second is documented close to the hinge in the forelimb and strikes NW-SE (140° E) after unfolding (Fig. 5, sites 670, 672). Unfortunately, these two sets were not identified at the same site, thus no relative chronological relationship could be established. A last set of joints and veins striking E–W after unfolding was documented in the forelimb of the fold (site 670) and abuts on fractures striking 140° E. No chronological relationship between this E–W striking set and the 110° E striking set was observed.

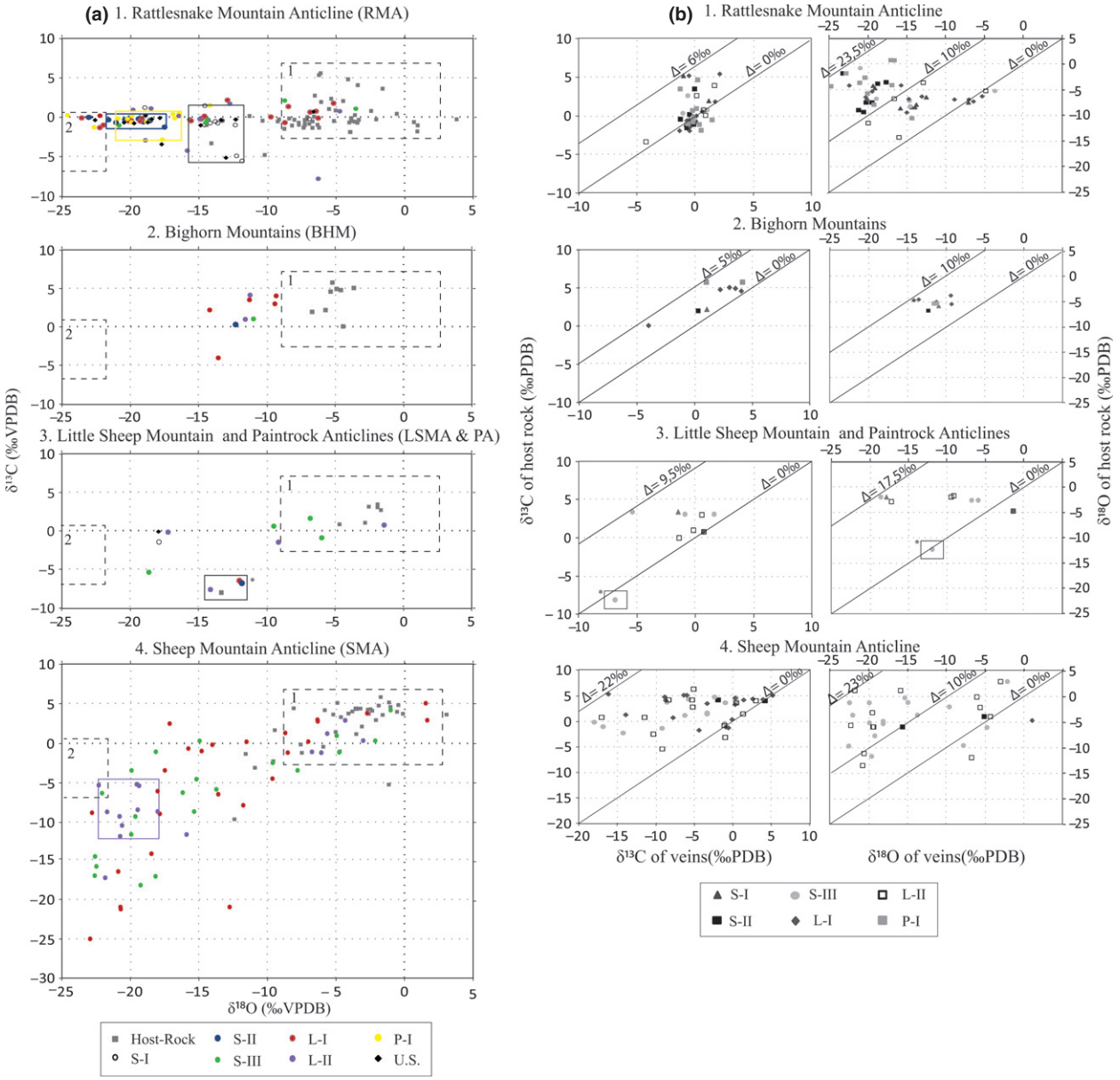

Fig. 10. (a) $\delta^{18}O$ vs $\delta^{13}C$ isotopic values for veins (reported as coloured circles and dots for each fracture sets) and host-rocks (squares) in the different structures reported on Fig. 1, except Elk Basin. The Carboniferous limestone isotopic range after Katz *et al.* (2006) was reported as dotted frame 1 along with the isotopic signatures for hydrothermal fluids derived from meteoric fluids as dotted frame 2. The latter was calculated from Palaeogene fluids (Koch *et al.*, 1995) by using the precipitation equations for $CaCO_3 \leftrightarrow H_2O$ (Zheng, 1999). Data set from Sheep Mountain Anticline is after Beaudoin *et al.* (2011). (b) $\delta^{13}C$ vein calcite vs the $\delta^{13}C$ limestone host-rock and $\delta^{18}O$ vein calcite vs $\delta^{18}O$ limestone host-rock in the same studied structures. Solid lines and reported values are the isotope shift related to the degree of isotopic disequilibrium between vein cements and host-rock, $\Delta = 0‰$ being equilibrium. All values expressed in ‰ Pee Dee Belemnite.

The sedimentary cover of the BHM displays 3 sets of bed-perpendicular joints and veins (Fig. 6). The oldest set is poorly documented at the fold-scale (Fig. 6, site 733). It is composed of joints and veins striking 110° E (after unfolding), on which abuts the second set including joints and veins oriented NE–SW. This third set comprises joints and veins oriented NW–SE abutting on veins NE–SW (Fig. 8c), striking parallel to the main trend of the BHM hinge.

With regard to the scarcity of measurement sites on each fold, the complete description of a fold-scale fracture pattern remains impossible. However, because results of fracture analysis from individual fold structures are consistent between each other and are in agreement with previous detailed studies on SMA and RMA (Bellahsen *et al.*, 2006a; Amrouch *et al.*, 2010; Beaudoin *et al.*, 2012), we can reliably consider that the first-order characteristics of fracture development at the basin scale (orien-

tations, mode of deformation and sequence) were captured. Indeed, fracture populations and their succession through time are quite similar in each fold, with a common 110° E fracture set, followed by NE–SW and then by a NW–SE (parallel to fold hinges) set. A second-order set is observed in EB (Fig. 5, Site 670). This late pre-folding set of fractures striking E–W probably reflects local conditions of structural evolution of the EB and will not be further considered in our discussion addressing basin scale features.

Petrography and mineralogy of veins at fold-scale

X-ray diffractometer analyses of vein cements highlight mineralogical differences between veins and host-rocks in most cases (Fig. 9). Indeed, host-rocks exhibit three types of mineralogy: pure dolomite (Fig. 9a, c, Bighorn, Phosphoria and Madison Formations), dolomite mixed with small amount of quartz (Tensleep), and quartz and calcite in variable amounts (Fig. 9b, Flathead, Gros Ventre, Gallatin, Cloverly and Morrison and Mowry Formations). On the other hand, veins (0.1–3 cm thick) mainly contain calcite, with a variable amount of quartz when the host-rock is sandstone, everywhere in the basin and in all sets (Fig. 9). The microscopic observations of calcite veins stained with red-S alizarin and iron ferricyanid reveals that no vein contains ferroan calcite (Dickson, 1966). Microscopic observations were also used to confirm mode I opening of veins (Fig. 7) and to identify sheared veins and multi-opened veins, which were not analysed (see below). X-ray diffraction analyses and observations under cathodoluminescence also highlighted that some host-rocks and veins contain both calcite and dolomite (Fig. 9b). Such infrequent samples (4) have not been analysed geochemically, because we cannot ascertain that the calcite precipitated from a single fluid during an unique event.

Various petrographic features can be observed in veins, fibrous and nonfibrous veins being observed anywhere with no difference according to which fold is considered. As we aim at deciphering fluid flow in relation to fracture development in a well-defined tectonic framework, we only studied mode I veins with a single phase of cement. In addition to some crack-seal (as defined by Ramsay, 1980) and shear veins, that are poorly encountered, we observe in all folds ataxial, antitaxial, syntaxial and blocky calcite veins (in the sense of Hilgers & Urai, 2002; Bons *et al.*, 2012). Most studied veins appear to be blocky calcite veins, some present antitaxial fibrous calcite, while other types remain scarce. In most cases, textures of luminescence of veins thoroughly contrast with the luminescence of host-rocks (Fig. 7).

At RMA, 3 petrological types can be defined, all representing a specific precipitation condition, independently from fracture sets. (1) Antitaxial veins, exhibiting bridge-

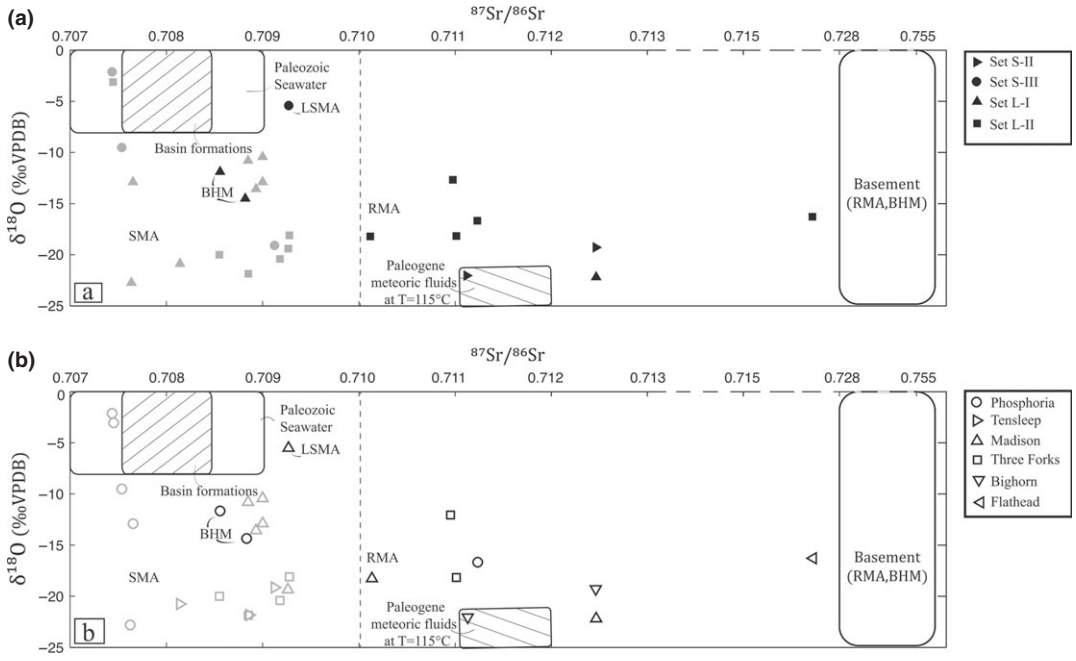

Fig. 11. Strontium ($^{87}Sr/^{86}Sr$) vs oxygen isotope (‰ Pee Dee Belemnite) crossplot of calcite veins according to fracture set (a) or to sedimentary formation (b). Strontium isotope values for Palaeozoic seawater are after Veizer *et al.* (1999) and Bruckschen *et al.* (1999), while Palaeozoic/Jurassic basin formations and Palaeogene meteoric values are from Rhodes *et al.* (2002). Framed labelled 'basement' represent minimal range of values measured in granitic rocks at Rattlesnake Mountain Anticline and Bighorn Mountains. The dashed lines represent the maximal value measured in the eastern portion of the basin and the minimal value measured in the western part of the basin. Light grey symbols represent data from previous studies at Sheep Mountain Anticline (Katz *et al.*, 2006; Beaudoin *et al.*, 2011; Barbier *et al.*, 2012a,b).

like crystals (Fig. 7a), are filled with material characterized by an orange calcite-related bright luminescence. The homogeneity of this luminescence indicates a constant precipitation rate for fluid during stable oxidation–reduction conditions (e.g. from LSMA, Fig. 7h). These veins witness a fluid precipitation coeval with fracture opening. In some cases, the luminescence is the same as in the surrounding host-rocks, implying the presence of common activators (in term of nature and volume) in crystals of veins and host-rocks, which could likely be related to chemical equilibrium during the precipitation of vein filling. (2) Some blocky calcite veins are mainly filled with material exhibiting a zoned orange calcite-related, bright to dull luminescence: the zonation (Fig. 7e) shows that the crystals precipitated from a single fluid, with variation in the precipitation rate or/and oxidation-reduction conditions. These calcite veins witness crystal growth in an opened or opening fracture. (3) Some veins contain two phases of blocky calcite cement, their borders consisting of thick fringes with a red-orange and homogeneous bright luminescence, while their central parts consist of crystals with heterogeneous patchwork of nonluminescent, bright orange and dull red-orange luminescent crystals (e.g. in BHM: Fig. 7f); such a setting witnesses two phases of vein opening. On the contrary, when the border between two generations of vein cements displays an irregular shape, dissolution of the first cementation phase before or during the second cementation phase is more likely (e.g. Beaudoin *et al.*, 2011). The latter were not studied because we consider those vein cements as not suitable to identify a fluid system unambiguously related to a given fracture set development. Alternatively, host-rocks display two textures of luminescence: (1) a red, homogeneous bright luminescence in partially to completely dolomitized limestones and (2) an orange homogeneous bright luminescent calcite cementing quartz grains in sandstones.

In thin-sections from BHM, calcite veins display crystals with a high density of thin twins in every setting. These veins are either (1) antitaxial veins filled with an orange, homogeneous dull or bright luminescent calcite or (2) blocky calcite veins, characterized by a heterogeneous bright to dull orange luminescence (Fig. 7f). The latter type exhibits a thin fringe of small crystals of calcite witnessing the very beginning of precipitation during the opening of the veins, which indicates a rate of opening that exceeds the precipitation rate (e.g. Hilgers & Urai, 2002; Bons *et al.*, 2012). A last vein-type is encountered in BHM: (3) multi-opened blocky calcite veins exhibiting borders consisting of thin fringes with a red-orange and homogeneous bright luminescence (Fig. 7f). As in all folds, this type of vein was not considered suitable for the reconstitution of a fluid system as it cannot be unambiguously related to a given fracture set. Host-rocks display two kinds of petrological settings: rocks from the Phosphoria Formation consist of oolithes and cements displaying a red, dolomite-related, homogeneous and bright luminescence, while rocks from the Madison Formation consist of dolomudstone displaying a red, homogeneous bright luminescence.

In thin sections from LSMA, two different textures of luminescence are observed in calcite veins: (1) The most commonly observed texture is blocky calcite veins displaying a high density of thin twins. An orange, calcite-related heterogeneous luminescence without growth-related zonation is systematically present in this petrological setting (Fig. 7g). (2) Some antitaxial veins are present, displaying single cement with homogeneous orange bright luminescence texture. Host-rocks mainly consist of dolomudstones, displaying a red, homogeneous bright luminescence. Some portion of host-rocks contains locally minor amount of calcite, displaying an orange, homogeneous dull luminescence.

In thin sections from PA, a single petrological type is observed: ataxial veins filled with bridge-like crystals of calcite that display an orange, homogeneous bright luminescence, which has the same luminescence as the calcite cementing the quartz grains in the host-rocks (Fig. 7d, h).

Geochemical characterization of fold-scale palaeohydrogeology

Isotopic analyses of oxygen and carbon were performed on both veins and related host-rocks when the latter contain $(Mg)CaCO_3$ (dolomite or calcite) in RMA, LSMA, PA and BHM. $\delta^{13}C$ and $\delta^{18}O$ values of cements are plotted according to the fracture set together with the $\delta^{13}C$ and $\delta^{18}O$ values of host-rocks (Fig. 10a). Each diagram represents the isotopic signatures of veins and host-rocks in a single fold, except one that represents data of LSMA and PA. Previously published results obtained in cements of veins and host-rocks of SMA (Beaudoin *et al.*, 2011) are also reported in Fig. 10a. To discuss the degree of isotopic equilibration between veins and host-rocks, $\delta^{18}O$ values of cements are plotted against $\delta^{18}O$ values of their respective host-rock according to the fracture set (Fig. 10b); the same is done with $\delta^{13}C$ values. Strontium isotopic ratios $^{87/86}Sr$ were measured in 11 vein cements and are plotted against $\delta^{18}O$ values of these cements (Fig. 11) according to fracture sets (Fig. 11a) and to formations (Fig. 11b). These new data are reported along with previously published values relative to veins of SMA (Katz *et al.*, 2006; Beaudoin *et al.*, 2011; Barbier *et al.*, 2012a, b) and of RMA (Katz *et al.*, 2006). Strontium isotopic values of host-rocks are also reported for the Bighorn Formation at RMA and for the basement rocks at RMA and BHM (this study).

Microthermometric measurements were performed in primary and secondary fluid inclusions of vein cements to estimate the minimum filling (entrapment) temperature of fluids thanks to the homogenization temperature (Hanor, 1980) and to characterize salinity of fluids thanks to RAMAN microspectrometry. Results are presented as histograms gathering data from this study and those previously published data for SMA (Beaudoin *et al.*, 2011).

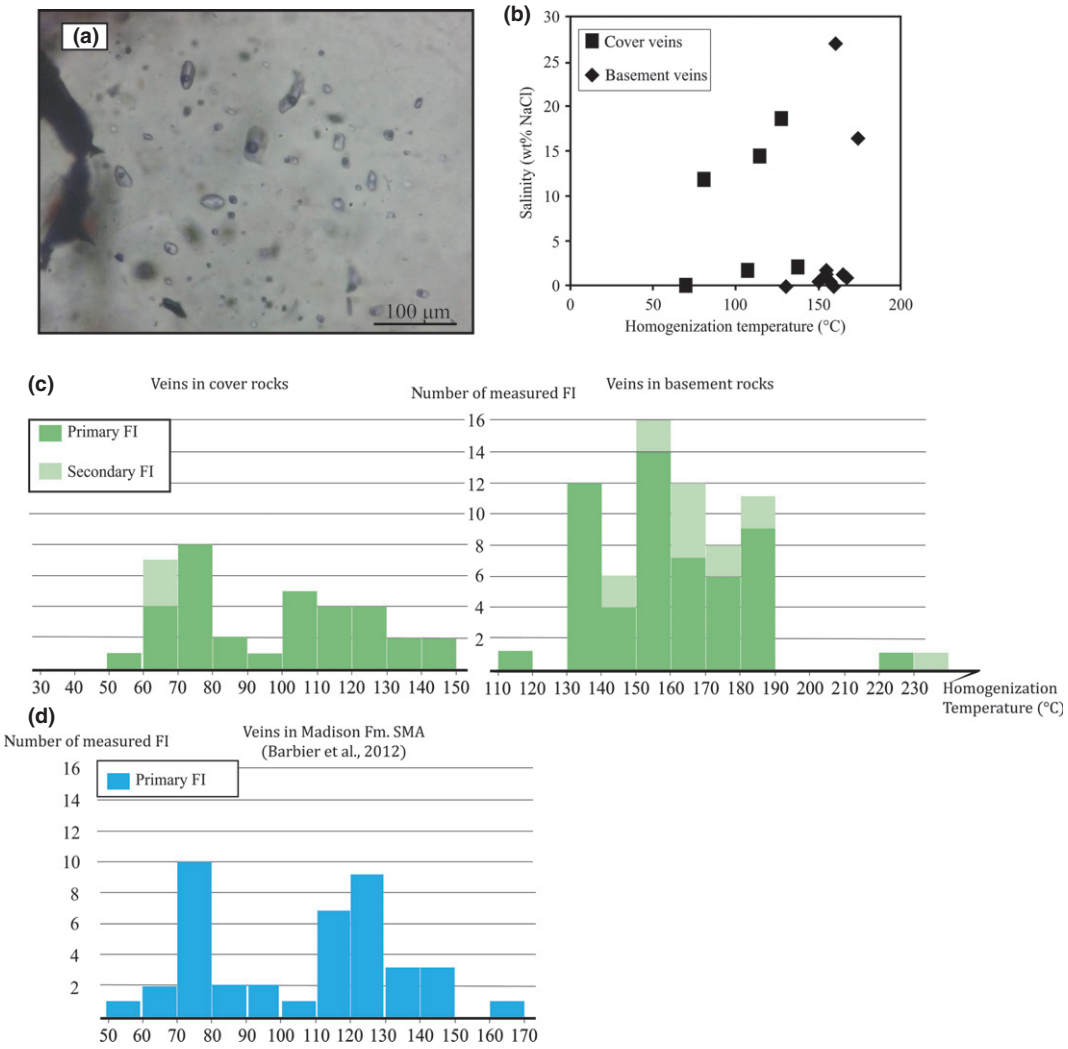

Fig. 12. (a) Photomicrograph of a primary fluid inclusion assemblage in quartz of a vein from basement rocks. (b) Salinities (in mass %NaCl) measured by RAMAN microspectometry vs homogenization temperature measured in the same fluid inclusion in calcite or quartz veins of the cover rocks (squares) and basement rocks (diamonds). (c) Histograms of distribution of homogenization temperature measured in primary and secondary fluid inclusions in veins of both the cover and the basement. Data from all structures were compiled together on this histogram. (d) Comparison with histogram of distribution of homogenization temperature measured in primary fluid inclusions in vein calcite of the Madison formation, from the canyon of Sheep Mountain Anticline (Barbier *et al.*, 2012a, b)

Homogenization temperatures are also plotted against salinity (Fig. 12) and against $\delta^{18}O$ values of the precipitated fluid according to the $\delta^{18}O$ ratios of their respective cements (oblique line, Fig. 13). In contrast to the work reported in Beaudoin *et al.* (2011) where calculations of the $\delta^{18}O$ of fluids were performed considering the $H_2O \leftrightarrow$ Calcite fractionation factor from Kim & O'neil (1997), the fractionation factor used hereinafter is that of Zheng (1999). This choice has been motivated by the study by Coplen (2007), which emphasizes that the fractionation factor from Kim & O'neil (1997) was underestimated by 1.5‰. Thus, fractionation factor developed by Zheng (1999) seems to be closest to real fractionation considering stable oxygen isotopic equilibrium.

Results are presented hereinafter according to structure location in the BHB: first RMA, located in the western edge of the basin and then the structures from the eastern part of the basin, LSMA, BHM and PA.

Western part of the BHB

At RMA (Fig. 10a), veins and host-rocks exhibit a wide range of oxygen isotopic signatures ($-24.8‰ < \delta^{18}O < -3.5‰$ PDB for veins; $-14.5‰ < \delta^{18}O < +4‰$ PDB for host-rocks) and a narrower range of carbon isotopic signatures ($-7‰ < \delta^{13}C < +2‰$ for veins; $-4.8‰ < \delta^{13}C < +5.2‰$ PDB for host-rocks). Isotopic signatures of host-rocks (grey squares on Fig. 10a) seem to vary according to formations (see Table S1). Indeed, host-rocks from the Flathead, Gros Ventre, Gallatin and some of the Bighorn Formations (i.e. from Cambrian to Ordovician rocks), range from −8.5‰ to −6.5‰ for stable oxygen isotope and from −1.7‰ to 0‰ for stable

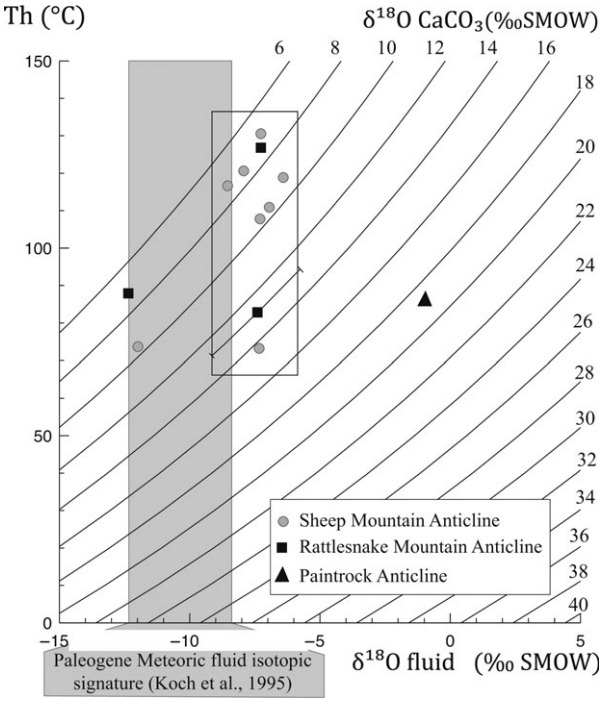

Fig. 13. $\delta^{18}O$ isotopic values of vein calcite (Standard Mean Ocean Water (SMOW), oblique lines) vs $\delta^{18}O$ isotopic values (SMOW) of fluids, calculated as a function of crystallization temperature, approximated by homogenization temperatures measured by fluid inclusion microthermometry. The calculations were made by using precipitation fractionation equation in Zheng (1999).

carbon isotope. The rest of the Bighorn Formation host-rocks along with carbonate portion of host-rocks from the Three Forks Formation (i.e. from Ordovician to Devonian) range from −4.5‰ to −2‰ and from −2‰ to +1‰ for $\delta^{18}O$ and $\delta^{13}C$ respectively. At last, the host-rocks belonging to Madison and Phosphoria Formations (i.e. Mississippian and Permian times) range from −6.5‰ to −1.5‰ for $\delta^{18}O$ and from +1.8‰ to +5.5‰ for $\delta^{13}C$.

According to $\delta^{18}O$ isotopic values, most of vein cements precipitated from nonlocal fluids at higher temperature than surrounding host-rocks (>75% of data with a minimal difference Δ of 5‰, Fig. 10b). Clear differences arise in isotopic signatures according to vein sets: vein cements from set S-I (black circles in Fig. 10a) exhibit isotopic signatures that range from −20‰ to −7‰ for stable oxygen isotope and from −5.5‰ to +1.5‰ for stable carbon isotope. Most of the isotopic values for these veins are, however, distributed in a narrower range (black frame: 11 veins out of 14; $-15.5‰ < \delta^{18}O < -12.5‰$; $-5.2‰ < \delta^{13}C < +1.5‰$). Isotopic values from set S-II vein cements (blue dots, with blue frame on Fig. 10a) range from −23‰ to −16.5‰ for stable oxygen isotope and from −2.8‰ to +0.5‰ for stable carbon isotope. Veins from set S-III (green dots) were poorly sampled, because they were poorly represented at the fold scale (Beaudoin *et al.*, 2012); they have isotopic signature scattered from −20.5‰ to −3.5‰ for oxygen and from −0.7‰ to 2‰ for carbon. Isotopic values related to set L-I veins (red dots) cover a wide range ($-23.5‰ < \delta^{18}O < -5.5‰$; $-1.5‰ < \delta^{13}C < +1.5‰$) with veins distributed in three narrower ranges of oxygen isotopic values ($-23.5‰ < \delta^{18}O < -19‰$, $-15.5‰ < \delta^{18}O < -13‰$ and $-10‰ < \delta^{18}O < -5‰$). Vein cements from set L-II (purple dots) display isotopic signatures that are scattered between −20‰ and −5‰ for $\delta^{18}O$ and between −7‰ and +1.5‰ $\delta^{13}C$. The $\delta^{18}O$ isotopic values of cement filling veins belonging to set P-I (yellow dots) range between −23.5‰ and −13‰. Most of the P-I cements isotopic values remained confined to a narrower range between $-21‰ < \delta^{18}O < -17‰$, and $-2‰ < \delta^{13}C < -0.5‰$ (yellow frame on Fig. 10a).

$^{87/86}Sr$ ratios of vein cements in RMA range between 0.7102 and 0.7123 for veins in Bighorn, Three Forks, Phosphoria and Madison Formations, and reach 0.7159 in Flathead Formation (Fig. 11). The basement rocks cropping out at RMA were also analysed and show values ranging from 0.7284 to 1.016. The latter value, exceeding an isotopic ratio of 1, stresses a high concentration of K-feldspar in the analysed sample.

At RMA, most of the fluid inclusions in carbonate veins are single-phase and composed of fresh fluid (with zero salinity). Two different fluids are highlighted by homogenization temperature and salinity of two-phase inclusions: a bimodal distribution of homogenization temperatures (Th) (for both primary and secondary) around 75 °C and 125 °C and two modes of salinities, which are around 0% and around 17% mass NaCl. Fluid inclusion populations in particles of quartz from veins and host-rocks in Precambrian basement rocks and Cambrian sandstones of the Flathead Formation were also studied, and a unimodal distribution of Th is exhibited, with a mode around 150 °C in veins and 160 °C in host-rocks.

Eastern part of the BHB

In LSMA (Fig. 10a), veins are distributed in two distinct groups characterized by different ranges of $\delta^{18}O$ despite the small amount of data: a first group with depleted cements ($-10‰ < \delta^{18}O < -5‰$), comprising only sets S-III and L-I veins and a second group with more depleted cements comprising all studied sets ($-18.5‰ < \delta^{18}O < -17.5‰$). Meanwhile, host-rocks of the Madison Formation exhibit a narrow range of isotopic signatures ($-4.8‰ < \delta^{18}O < -1.7‰$; $+0.3‰ < \delta^{13}C < +4‰$). Stable oxygen and carbon isotopic signatures of veins are clearly different from their respective host-rocks ones, exhibiting two distinct degrees of host-rock buffering (Δ value, Fig. 10b): the first one reflects moderate buffering, with a Δ value ranging between 5‰ and 10‰, while the second one reflects weak buffering, with a Δ value ranging between 15‰ and 17‰ (Fig. 10b). $^{87/86}Sr$ ratio was measured in a vein of set S-III buffered by host-rock, displaying a radiogenic value of 0.7092. Veins contain mainly single-phase fluid inclusions and only few

two-phase fluid inclusions, which were unsuitable to perform microthermometric measurements because of their size (<5 μm). Moreover, calcite crystals exhibit a high natural fluorescence, limiting RAMAN measurement to only a single primary fluid inclusion, displaying a salinity of 0% (mass NaCl).

Few veins were found in fracture sets observed in PA (Fig. 10a, black frame on third chart), the related $\delta^{18}O$ and $\delta^{13}C$ values are distributed in a narrow range with the same values as in host-rock cements (Jurassic sandstones of the Cloverly and Morrison Formation, $-14‰ < \delta^{18}O < -12‰$; $-8‰ < \delta^{13}C < -6‰$). Microthermometry of primary fluid inclusions performed in the calcite cement of a L-I sample highlights a unimodal distribution of Th around 70 °C, along with an important population of monophasic fluid inclusions.

In BHM (Fig. 10a), isotopic signatures of all the veins are distributed in a narrow range ($-14.5‰ < \delta^{18}O < -9‰$; $-4.5‰ < \delta^{13}C < +4.5‰$) that is distinct from isotopic values of the host-rocks from Madison and Phosphoria formations ($-6.5‰ < \delta^{18}O < -4‰$; $0‰ < \delta^{13}C < +6‰$). Fig. 10b shows a systematic minimal isotopic difference between veins and host-rocks of 6‰ for $\delta^{18}O$ and between 1‰ and 4‰ for $\delta^{13}C$. $^{87/86}Sr$ ratios were measured on two different veins of set L-I of the Phosphoria formation and results display low radiogenic values ranging from 0.7084 to 0.7088, while granitic basement rocks of the BHM exhibit a radiogenic $^{87/86}Sr$ ratio of 0.7556. Like at LSMA, veins have plenty of monophasic or leaked fluid inclusions (<5 μm) and calcite displays a high fluorescence, which prevents measurement using RAMAN microspectrometry; so the salinity was measured only once in a primary single-phase fluid inclusion, revealing a 0% mass NaCl in a vein from set P-I.

In SMA, new measurements of aqueous and oil-bearing fluid inclusions in the Madison and Phosphoria Formations (Table 2) support previously published measurements at fold-scale (Beaudoin *et al.*, 2011). Indeed, the microthermometry of primary aqueous fluid inclusions highlights a distribution of homogenization temperatures with a mode around 130 °C and newly performed RAMAN analyses show that those fluids have zero salinity. Microthermometry has been performed on oil-bearing fluid inclusions in the Phosphoria Formation, and the unimodal distribution of homogenization temperatures (about 70 °C) is consistent with results from the study of the Madison Formation by Barbier *et al.* (2012a, b). Unfortunately, the scarcity of aqueous fluid inclusions developed coeval with these oil-bearing fluid inclusions precludes any reconstruction of pressure and temperature conditions of precipitation.

Synthesis of geochemical results at the basin scale

$\delta^{18}O$ and $\delta^{13}C$ values, $^{87/86}Sr$ ratios and microthermometric measurements highlight that fluid systems in each fold seem common at the basin scale (Figs. 10, 11 and 12), a similar type of fluid signatures being documented in the eastern part of the BHB (this study and Beaudoin *et al.*, 2011) and in western part of the BHB (this study). Three distinct ranges of $\delta^{18}O$ values for fluids can be observed, along with distinct homogenization temperatures measured in fluid inclusions (Fig. 12). The homogeneity of the calculated $\delta^{18}O_{fluids}$ for most of the samples (Fig. 13) suggests that the depletion of $\delta^{18}O$ of the vein-filling calcite can be interpreted as primarily controlled by the fluid temperature during precipitation. Hereinafter, we will consider burial estimates and reconstructed geothermal gradient of about 25 °C km^{-1} (Brigaud *et al.*, 1990). Based on stable oxygen isotopes and homogenization temperatures, the first group of cements reflects precipitation from fluids at isotopic equilibrium with host-rocks ($-9‰ < \delta^{18}O < 0‰$). The second group exhibits $\delta^{18}O$ signatures slightly more depleted than those of the host-rocks, but which reflect a precipitation temperature consistent with burial according to the measured homogenization temperature ($-17‰ < \delta^{18}O < -12‰$; Th = 80 °C). The last group of vein-filling is characterized by very depleted $\delta^{18}O$ signatures and by homogenization temperatures significantly higher than those of the surrounding environment ($-23‰ < \delta^{18}O < -18‰$; Th > 120 °C). The latter group reflects crystals precipitated from hydrothermal fluids (in the sense of Machel & Lonnee 2002), i.e. referring to crystals that precipitated from fluids flowing at a temperature significantly higher than the one of the strata, with no genetic implication for fluid source. One can also observe that at both SMA and RMA, the highest $^{86/87}Sr$ ratios were measured in veins where calcite precipitated from hydrothermal fluids.

DISCUSSION

Microstructural evolution of the BHB

The main fracture sets defined at the fold-scale are consistent at the basin scale. Indeed, very few fracture sets are uncorrelated with the fracture sequence defined at SMA (Bellahsen *et al.*, 2006a; Amrouch *et al.*, 2010) and RMA (Beaudoin *et al.*, 2012):

The oldest fracture set contains fractures striking mainly E–W (Set S-I, Fig. 8). According to previously published results (Beaudoin *et al.*, 2012), this fracture set can be related to an early Sevier LPS stage. This set is well represented at RMA (i.e. the western part of the BHB), while it is poorly developed at SMA. Set S-I is also documented at LSMA (Fig. 3), but is absent from PA and BHM. Thus, eastward inhibition of the development of the set S-I is consistent with the western location of the Sevier fold-thrust belt and with the eastward basin-scale stress attenuation emphasized in Beaudoin *et al.* (2012).

N-S fractures were described at EB (Fig. 5, site 669), and cross-cutting relationships imply that this set predates Laramide sets L-I and L-II (see below); as a result, this fracture set is similar to set S-II described at RMA, and is probably related to flexure

Table 2. Temperature and salinity of fluid inclusions

Sample	Set	Formation	Location	Number of inclusions measured	Type of fluid inclusion	Homogenization temperature (°C)	Salinity (% mass NaCl)	∂18O (‰PDB)	Note
D11	L-I	Sundance	Paintrock A.	10	Primary	69.2–82	UM	−12.6	
LSM09	L-II	Madison	Little Sheep M. A.	2	Primary	UM	0	−17.21	Size <5 μm
BM 17	P-I	Madison	Big Horn Mountains	3	Primary	UM	1	−12.3	Size <5 μm
R93	L-II	Madison	Rattlesnake Mountain A.	5	Primary	<50	0	−20.16	Monophasic population
				3	Secondary	<50	0–5.37	−20.16	Monophasic population
R104	L-I	Three Forks	Rattlesnake Mountain A.	5	Primary	69.4–127.2	0–18.63	−22.27	
				2	Secondary	66–68	UM	−22.27	
R117	S-II	Gallatin	Rattlesnake Mountain A.	2	Primary	60.9–93	UM	−17.76	
R139	P-I	Madison	Rattlesnake Mountain A.	2	Primary	<50	6.7		Monophasic population
R149	S-I	Basement	Rattlesnake Mountain A.	19′	Primary	131–290.5	UM	UM	
				17′	Secondary	92–297.5	UM	UM	
R183	L-II	Basement	Rattlesnake Mountain A.	6′	Primary	UM	6.45–28.52	UM	
R198	S-I	Basement	Rattlesnake Mountain A.	28′	Primary	136–225	0–1.62	UM	
				3′	Secondary	160–174	0.96–27.25	UM	
S10	L-II	Madison	Sheep Mountain A.	6	Primary	130–147.5	0	−20.78	
13	L-I	Phosphoria	Sheep Mountain A.	1	Primary	91.6	UM	−17.89	
				50	Primary	30–83.3	UM	−17.89	Oil-bearing F.I.
				20	Secondary	25–60.5	UM	−17.89	Oil-bearing F.I.
09	L-I	Phosphoria	Sheep Mountain A.	4	Primary	120.9–146	UM	−12.77	
Beaudoin *et al.* (2011									
18	3	Tensleep	Sheep Mountain A.	4	Primary	113–124	UM	−20.82	
V1-2	2	Phosphoria	Sheep Mountain A.	3	Primary	107–135	2.1–14.4	−22.81	
47	2	Tensleep	Sheep Mountain A.	2	Primary	115–116	UM	−22.935	
13	2	Phosphoria	Sheep Mountain A.	2	Primary	71.5–72.2	UM	−17.89	
				5	Primary	98.6–202	UM	−17.89	Oil-bearing F.I.
45	U.S.	Phosphoria	Sheep Mountain A.	6	Primary	105.3–110.5	2–2.8	UM	
Katz *et al.* (2006)*									
SM 1.95 m	N.D.	Madison	Sheep Mountain A.	39	Primary	120–140	Low	−22.7	
Barbier *et al.* (2012a, b)*									
SM4.38	N.D.	Madison	Sheep Mountain A.	31	Secondary	32–67.5	N.D.	−20.27	Oil-bearing F.I.
				13	Primary	51–57	N.D.	−20.27	Oil-bearing F.I.
SM2.08	N.D.	Madison	Sheep Mountain A.	77	Primary	65–85	N.D.	N.D.	
				12	Primary	40.5–82	0.5	N.D.	Oil-bearing F.I.
SM5.08	N.D.	Madison	Sheep Mountain A.	40	Primary	41–69	N.D.	−15.62	Oil-bearing F.I.
				2	Primary		0.2–0.4	−15.62	

All temperatures coming from this study are given ±0.5 °C.

*These values are related to cemented veins in Madison Fm at SMA.

N.D. is for "no data provided in the literature", UM is for "unable to measure". Prime symbols indicate fluid inclusions measured in quartz.

migration during the formation of the foreland basin. EB being in the northern part of the BHB, the occurrence of set S-II is consistent with the findings of Beaudoin *et al.* (2012) who proposed that the Sevier flexure imprinted more significantly the western part of the basin, the orogenic load (the Sevier Range) being located to the west (Decelles, 2004).

Set 110° E (S-III), Set NE–SW (L-I) and Set NW–SE, striking parallel to the fold hinge (L-II), are observed at nearly all structures except in Elk Basin, where set S-

III is missing. However, set S-III joints and veins abut on set S-I and are present in all the other studied folds. It has been related to a late Sevier stage (Amrouch *et al.*, 2010) that affected the whole BHB.

Chronological relationships (Fig. 8) also are consistent at basin scale, illustrating a coeval development of fracture sets related to Laramide tectonic event (L-I and L-II). As proposed in previous studies (Bellahsen *et al.*, 2006a, b; Amrouch *et al.*, 2010, 2011; Beaudoin *et al.*, 2012), sets L-I and L-II are probably related to the Laramide contractional event, with set L-I reflecting early folding LPS and set L-II being syn-folding and related to local curvature of strata at fold hinges.

The consistency of data from individual folds allows to confidently propose a scenario of fracture development that is relevant at the scale of the entire BHB. There was a significant strain decrease from west to east during the early Sevier LPS (namely Set S-I, well-developed at RMA, less to poorly developed at LSMA and SMA/PA and absent at BHM), which could be related to the increasing distance to the Sevier deformation front located west of the basin. The eastward propagation of this Sevier thrust belt was also well recorded in the still horizontal strata of the foreland, regarding the consistent development at the regional scale of the late Sevier LPS-related set S-III. At the basin scale, our data set also suggests a wide distribution of Laramide fracture populations, which can be related to a fast propagation of the Laramide front of deformation across the BHB, as suggested by thermochronological studies that support an early uplift of the Bighorn Mountain arch East of the BHB (Crowley *et al.*, 2002).

Mechanisms and timing of calcite precipitation in veins

The mechanisms for calcite precipitation from ascending hydrothermal fluids must be addressed, as calcite has a retrograde solubility, and so preferentially precipitates during increase in temperature. However, other parameters independent from temperature are of major importance for calcite precipitation (Bons *et al.*, 2012). pH and oxydo-reduction variations due to migration from depth to more surficial strata or to mixture of different fluids will affect the oversaturation of the fluid in Ca, enabling precipitation of fluids, even when ascending fluids are cooling down. Moreover, a sudden decrease in pCO_2 will also enhance calcite precipitation. Thus, the opening of joints can easily promote these mechanisms of precipitation, as it develops local pCO_2 decrease and as it can lead to fluid migrations (Bons *et al.*, 2012). These processes can explain why veins in sandstones and dolostones may contain newly formed calcite with fluid inclusions in thermal disequilibrium with host-rocks.

This would imply that the fluid precipitation is coeval with vein opening and that it depicts reliably fluid system at that time, as usually assumed in the literature (Dietrich *et al.*, 1983; Vandeginste *et al.*, 2012; Evans & Fischer, 2012). The petrological outline of veins can help constrain the timing of opening and precipitation (Hilgers & Urai, 2002): when antitaxial parts are present in veins, the precipitation rate equals or exceeds the opening rate, reflecting undoubtedly precipitation coeval with opening (Bons *et al.*, 2012). Unfortunately, a lot of veins in the BHB are filled with blocky calcite (Fig. 7), which indicates the precipitation of fluids in a void, due either to a fluid precipitating after joint development or to a fluid precipitating at slower rate than the rate of opening. The latter case can nevertheless reflect a coeval opening/precipitation timing if the precipitation is directly triggered to the opening of the veins, which can safely be assumed in the BHB. Moreover, with a fracture set reflecting given tectonic event, each joint/vein may develop during the entire duration of the tectonic event, and is unlikely to remain open during following tectonic events. Thus, blocky calcite veins can reasonably be considered as reflecting coeval vein opening/precipitation over the time span corresponding to the development of a given fracture set.

Along with the fact that a fracture set contains both veins and noncemented joints, it is noteworthy that joints may open during the whole duration of each tectonic. It suggests that the development of a fracture set can create a strong increase in strata hydraulic permeability and enable fluid migration even if joints are nearly coevally cemented by calcite precipitated from fluid advection. A likely hypothesis is to consider that fracture sets characterized by a low range of $\delta^{18}O$ reflect a precipitation possibly triggered by a decrease in pCO_2 during joint opening. In contrast, fracture sets that display a large range of $\delta^{18}O$ might either reflect a precipitation triggered by fluid mixing as assumed ahead, or successive events of precipitation related to multi-stage opening of a vein. To limit such an ambiguous interpretation, we choose to consider only veins exhibiting a single phase of filling without tectonic reopening for our interpretation. This way, it makes sense to consider that mechanism for calcite precipitation could be either a decrease in pCO_2 during opening of fracture or a fluid mixture due to fluid migration during the joint set development. Thus, most of the isotopic signature reflects fluid system during opening of joints/veins of each set.

Palaeohydrology of the BHB

Origin of fluids

As shown in part 3.3.3, fluid systems reconstructed in each fold are consistent at the basin scale. The main differences between RMA and SMA fluid systems are (1) carbon isotopic values and (2) timing of precipitation of hydrothermal fluids. Carbon isotopic values reach $-25‰$ PDB at SMA (Fig. 10a-4, Beaudoin *et al.*, 2011), but are mainly around $0‰$ at RMA (Fig. 10a-1). The highly depleted $\delta^{13}C$ of vein filling at SMA can be explained by exchanges between a ^{12}C-enriched source (possibly oil)

and fluids from which calcite precipitated in veins. Considering the depletion of $\delta^{13}C$ of fluids due to exchanges between $CO_{2\ (g)}/CH_{4\ (g)}$ from oil and $CO_{2\ (g)}$ from fluids along with the poor fractionation during calcite precipitation (Bottinga, 1969; Emrich *et al.*, 1970), the ^{12}C-enriched source can be the Palaeozoic oils of the BHB (Chung *et al.*, 1981). The source rock of these oils is the Permian Phosphoria formation where oil generation and migration started during Sevier times and were enhanced during Laramide deformation (Fox & Dolton, 1995). These oils are characterized by variable $\delta^{13}C$ ratios related to the thermal maturation state, the most depleted oil (in term of $\delta^{13}C$) witnessing a nonmicrobial sulphate reduction with negligible fractioning, in reservoirs where temperatures were over than 80–120 °C (Orr, 1974). Thus, a likely hypothesis to explain a $\delta^{13}C$ value of 0‰ of vein filling at RMA is a lack of isotopic exchange between hydrocarbons and fluids from which calcite precipitated in veins, in contrast to what probably happened in the eastern part of the basin. The lack of interaction between fluids and hydrocarbons at RMA appears in apparent contradiction to the numerous oilfields in this western portion of the basin (e.g. in Stilwell *et al.*, 2010). However, there is no oilfield west of RMA; this suggests that no westward large-scale migration of hydrocarbons occurred during Sevier and Laramide deformations. Alternatively, we observe that some samples exhibit an isotopic value for carbon which is in disequilibrium with their related host-rocks, being either more or less negative (Fig. 10a-1, b-1). These differences may reflect some local contamination by hydrocarbons during small-scale hydrocarbon migrations, or little oxidation or sulphate reduction processes affecting the organic matter in rocks.

At SMA, hydrothermal fluids have been interpreted as derived from Palaeogene meteoric fluids (Beaudoin *et al.*, 2011) mainly because the isotopic signature of sets S-III to L-II (i.e. the only studied sets) is consistent with isotopic signature of Palaeogene meteoric fluids (Koch *et al.*, 1995; Norris *et al.*, 1996; Morrill & Koch, 2002). With the identical range of $\delta^{18}O$ signatures (Fig. 9a1–4), the same hydrothermal fluids probably flowed, although at RMA earlier than at SMA. Indeed, they may have flowed as soon as Cretaceous times, as they were recognized in cements of set S-II veins interpreted as related to the Sevier foreland flexure, which affected strata at RMA during Turonian times (Decelles, 2004). This timing suggests that hydrothermal fluids probably derived from meteoric fluids, which have migrated at depth before they flowed upwards in strata during the formation of the flexural basin. Because Cretaceous and Palaeocene meteoric fluids have identical $\delta^{18}O$ values (Dettman & Lohmann, 2000, and references herein), the fluids characterized in the basin could be related either to Cretaceous or to Palaeocene meteoric fluids.

Despite a strong scattering of isotopic (O, Sr) signatures, and thermal and salinity values, most of vein calcites in the basin seem to have precipitated from a common fluid at different temperatures (Fig. 13). The wide range of oxygen and strontium isotopic data for veins and the salinity recorded in fluid inclusions can best be explained as a mixing between two distinct geochemical end-members (Fig. 10a, dotted frames): formational fluids and basement-derived hydrothermal fluids. Formational fluids refer to poorly radiogenic fluids (<0.709, Fig. 10) with a high salinity (>10% wt NaCl, Fig. 12b) and maximal precipitation temperatures consistent with the maximal burial depth of limestones in the basin (*ca.* 90 °C, Fig. 14). Considering that these formational fluids exhibit a high salinity (Fig. 12b), they probably derived from Palaeozoic seawaters (Katz *et al.*, 2006) that theoretically fill the pore spaces in sedimentary strata (Bjørlykke, 2010). The occurrence in strata of both (1) poorly radiogenic, hypersaline fluids precipitating at thermal equilibrium with host-rock (*ca.* 60 °C in eastern part of the basin and *ca.* 80 °C in western part of the basin, Fig. 14) and (2) poorly radiogenic, hypersaline fluids precipitating at higher temperature than that predicted by local thermal gradient in host-rock reflects two distinct pathways for formational fluids. Underlying strata compaction could have generated part of formational fluids, but this process appears to produce a very limited quantity of fluids (Deming *et al.*, 1990; Bjørlykke, 1993, 1999a, b). Thus, formational pore fluids could have more likely been mobilized during fracturing, or could have been mobilized in the deeper parts of the basin by compaction and during fracture development (basinal formational fluids). Then, they would have flowed (both laterally via matrix porosity and fractures and/or vertically via fractures) towards the edges of the basin thanks to their temperature and to hydraulic gradient created by the forebulge during Sevier and by the formation of the BHB during Laramide.

Basement-derived hydrothermal fluids precipitated with a homogenization temperature (Th) from 110 °C to 140 °C that cannot be explained by fluids mobilized in the sedimentary strata of the basin if considering a 25 °C km^{-1} geothermal gradient (Brigaud *et al.*, 1990). These Th values are considered as minimal temperatures of entrapment for fluids (Hanor, 1980). These fluids are also characterized by a zero salinity, an isotopic disequilibrium with host-rock (Figs 10 and 12), and a radiogenic value higher than the one related to fluid–rock interactions with Palaeozoic sedimentary formations of the basin (Fig. 10; Veizer *et al.*, 1999; Rhodes *et al.*, 2002). These radiogenic values are higher than the one of meteoric fluids that flowed in contact with exhumed basement rocks, which are considered as meteoric surface waters (Rhodes *et al.*, 2002). The highest radiogenic values recorded at RMA probably reflect fluids that interacted at depth with radiogenic felsic-rich basement rocks or basement-derived rocks (such as the basal part of the Cambrian Flathead Formation), as already suggested by Katz *et al.* (2006).

Radiogenic values of the granitic basement rocks display a uniform range in each part of the basin (0.728 at RMA and 0.756 at BHM). In contrast, a notable differ-

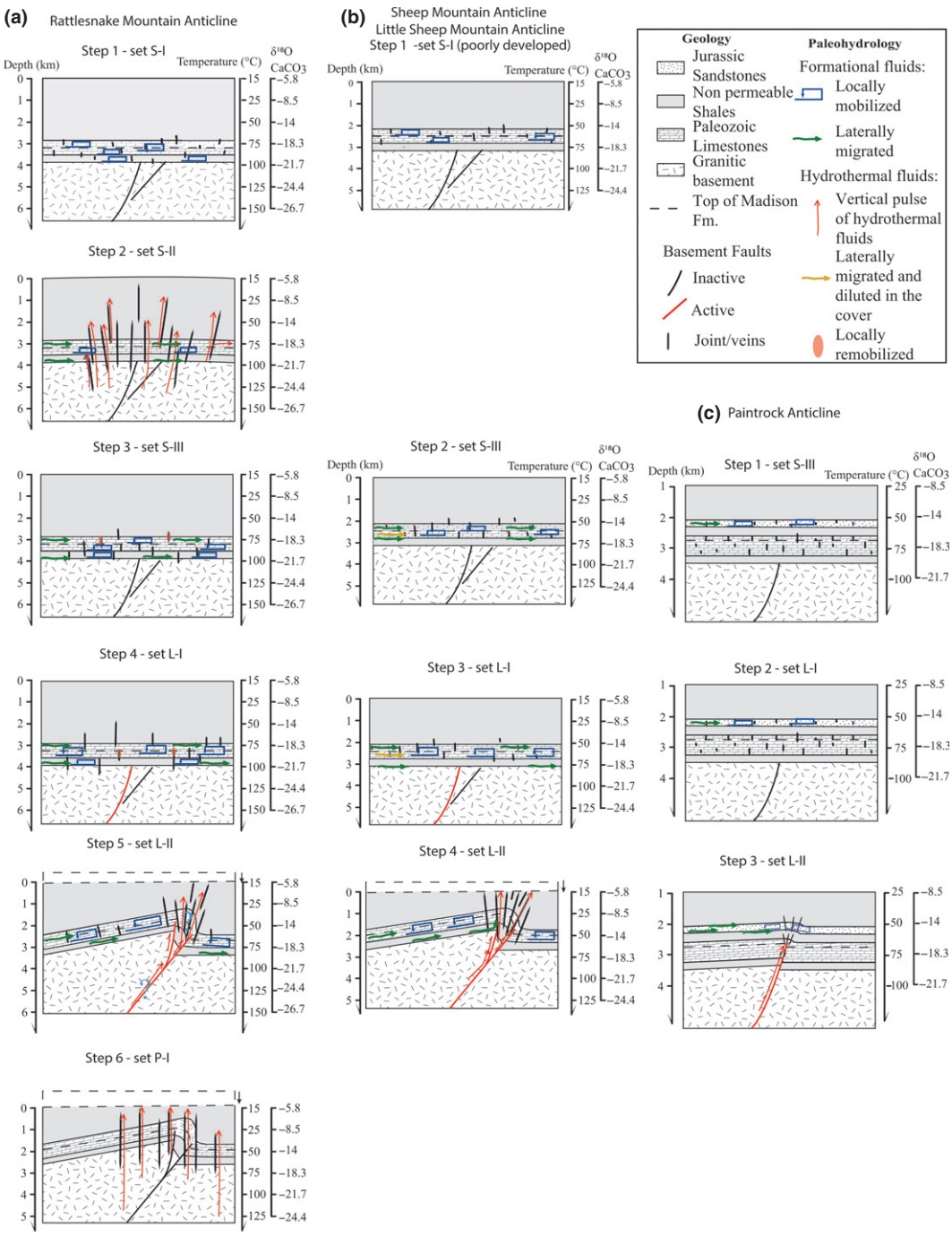

Fig. 14. Evolution of fluid system at the fold-scale (a) Rattlesnake Mountain Anticline (RMA), (b) Sheep Mountain Anticline (SMA)/Little Sheep Mountain Anticline(LSMA), (c) Paintrock Anticline (PA) during each step following the fracture sequence. The depths of burial are considered after sedimentary thicknesses from Darton (1905) for RMA, Hennier (1984) for SMA, Rioux (1994) for LSMA and Rogers et al. (1948) for PA, assuming a constant overburden until folding and thus a lack of Palaeocene sediment deposition on the edge of the basin (Fanshawe, 1971; Fox & Dolton, 1995). Syn-folding erosion was possibly less than 1 km due to fold growth (Amrouch et al., 2011) and is considered more effective after folding (between set L-II and P-I timing). If any, erosion is represented by a downward black arrow located on the upper right corner of the sketch. The temperature scale is consistent with a 25° km^{-1} geothermal gradient (Brigaud et al., 1990) and a surface temperature of 15 °C (Dettman & Lohmann, 2000 and references herein). Isotopic scale represents oxygen isotopic value of cement (expressed in ‰ Pee Dee Belemnite) precipitated from Cretaceous/Palaeogene meteoric fluids (after Koch et al., 1995; Norris et al., 1996; Bebout et al., 2001; Morrill & Koch, 2002) at different depths and temperatures. It integrates fractionation during precipitation calculated using Zheng (1999) equation of CaCO3 ↔ H2O and is consistent with palaeotemperature equation from Coplen et al. (1983). Thick black vertical segments represent fractures developing at each step of the fracture sequence, without representing previous ones. Red lines highlight periods of activation of thrust and décollement levels, blue, green and orange lines are related to palaeohydrology (refer to legend), and the dotted line in the cross-section refers to the top of the Mississippian Madison Fm.

ence arises when considering radiogenic values of vein calcites between the eastern part (<0.7092) and the western part of the basin (>0.7102). This difference, along with the similarity of the $\delta^{18}O$ values in each part of the basin, supports an eastward migration of highly radiogenic, hydrothermal basement-derived fluids progressively diluted by a low radiogenic medium such as the sedimentary cover and the formational fluids (e.g. Qing & Mountjoy, 1992).

The hypothesis developed hereinafter is to consider that most of the geochemical signatures of cements in all folds and fracture sets can be interpreted as resulting from a mixing between basement-derived fluids and formational fluids (Fig. 13). Thus, we tentatively describe the fluid history by simply considering a mix between the two end-members defined above. The wide isotopic (O, Sr) and thermal ranges of vein cements suggest different degrees of mixing between end-members and various degrees of fluid–rock interactions. During history of each fold, two main types of fluid systems are thus highlighted, one dominated by formational fluids (i.e. nonradiogenic hypersaline fluids with a $\delta^{18}O$ and Th consistent with basin temperature) and a second one dominated by basement-derived hydrothermal fluids (i.e. radiogenic and nonsaline fluids with a high Th and related cements that exhibits highly depleted $\delta^{18}O$ that cannot be explained by precipitation of formational basinal fluids considering the geothermal gradient and burial). The preserved high temperature and high radiogenic signature suggests a fast migration/precipitation of these fluids in strata. In contrast, the fluid system dominated by formational fluids where basement-derived hydrothermal fluids locally precipitated suggests a spatially variable rate of migration/precipitation.

Fold-scale fluid system evolution

At RMA, homogeneous $\delta^{18}O$ values of set S-I cements that range between $-12‰$ and $-16‰$ reflect a rather homogeneous fluid system (Fig. 10a1, black frame), which can be explained by a remobilization of local fluids at depth of 2–3 km (Fig. 14a). Thus, these homogeneity and values probably suggest a closed fluid system comprising mainly formational fluids from local reservoirs connected by joints from set S-I (e.g. Fischer *et al.*, 2009), precipitating at nearly thermal equilibrium with surrounding host-rocks, without trace of any basement-derived fluid (Fig. 14a).

In contrast, the highly depleted but low range of $\delta^{18}O$ values from $-19‰$ to $-22‰$ in set S-II veins (Fig. 10a1, blue frame) probably reflects precipitation of hydrothermal fluids (Fig. 14a). High strontium isotopic ratios (>0.712) measured in samples from set S-II suggest that the fluid system was no longer closed and that basement-derived fluids precipitated in veins during set S-II development (Fig. 11a). Moreover, set S-II is related to flexural forebulge development, so any burial between sets S-I and S-II is unlikely, which supports the interpretation of a system opening to basement-derived fluid at that time. The low range of depleted $\delta^{18}O$ of calcite precipitated from these fluids supports that they have avoided any efficient mixing with surrounding fluids and that they underwent limited diffusion with host-rocks during both migration and precipitation, suggesting that these processes occurred relatively fast (i.e. migration as a pulse).

Considering that the oldest characterized hydrothermal pulse occurred during the development of set S-II, the two successive fluid systems, during first set S-I and then S-II, are consistent with previous works (Travé *et al.*, 2007; Fischer *et al.*, 2009; Dewever *et al.*, 2011; Evans *et al.*, 2012), which pointed out that before the development of vertical drains in strata during deformation, the fluid system remains dominantly buffered by host-rock. The opening of the cover rock fluid system during flexure highlights that set S-II enhanced efficiently the vertical hydraulic permeability of the strata.

Set S-III fractures are poorly documented at RMA, making us unable to depict the fluid system prevailing during set S-III development. Cements from set L-I exhibit more scattered $\delta^{18}O$ values (Fig. 10), with highly radiogenic signatures (Fig. 11). The fluids from which precipitated the calcite, with highly depleted ($\delta^{18}O < -22‰$) and radiogenic ($^{87}Sr/^{86}Sr > 0.712$) isotopic signatures, are basement-derived hydrothermal fluids. To explain the precipitation in thermal disequilibrium of these fluids, an efficient vertical drain is required for them to flow into the sedimentary cover. Considering that these joints/veins developed during the early Laramide LPS stage (Bellahsen *et al.*, 2006a; Beaudoin *et al.*, 2012), it seems unlikely that a significant propagation of the thrust as well as a large amount of displacement along it occurred at that time. Thus, to explain the flow of basement-derived hydrothermal fluids in the cover, either the good vertical persistence of set L-I joints/veins through the cover of RMA allowed draining basement-derived fluids into the cover (Barbier *et al.*, 2012) or the few samples with $\delta^{18}O < -22‰$ reflect opening of veins later than the LPS during folding. Indeed, set L-I fractures are fold-axis perpendicular, which means that it is possible in theory that some joints related to this set developed at any time during the Laramide event. However, observed chronological relationships of set L-I assert that they often predate syn-folding set L-II (Bellahsen *et al.*, 2006a). In spite of these few samples, the large range of oxygen isotopic signatures measured in joints from set L-I can be interpreted as witnessing various mixing degrees between formational fluids and basement-derived fluids.

In set L-II, some $\delta^{18}O$ values of vein cements are depleted, with the same range as in set S-II (Fig. 10a, yellow frame), some are in the range of set S-II (Fig. 10a, black frame), while others are totally buffered by host-rocks. The Sr ratios suggest that some cements precipitated either from highly (up to 0.727) or poorly radiogenic fluids (Fig. 11). This scattered distribution witnesses that set L-II acted like set L-I, with various degrees of mixing

between local fluids and basement-derived hydrothermal fluids. This behaviour contrasts with the high hydraulic permeability of set L-II veins at SMA, acting as an important drain for the migration of basement-derived hydrothermal fluids in strata, namely at the fold hinge (Beaudoin *et al.*, 2011). Unfortunately, at RMA, the fold hinge is eroded or inaccessible, and there were few set L-II veins to study, so there is no reliable information to document the impact of the development of joints from set L-II on the palaeohydrological system. Again, the low number of data precludes us to reliably decipher the fluid system prevailing during folding at RMA, and data cannot be used to contradict the pulse of basement-derived hydrothermal fluids documented at SMA, which was related to outer rim extension joint development and to the reactivation/propagation of the basement thrust (Fig. 14) (Beaudoin *et al.*, 2011).

At last, P-I veins displayed cements characterized by homogenous and depleted $\delta^{18}O$ values comparable to set S-II ones (Fig. 10a, blue frame), which suggest another pulse of hydrothermal fluids that postdates the Laramide phase of the deformation. However, the absence of $^{87/86}Sr$ values precludes any distinction between basement-derived fluids and pore fluids from deep formations.

At LSMA, regarding stable oxygen isotopic signatures, the same scatter as at SMA (Fig. 10a) suggests that cements precipitated mainly from formational fluids, mixed partially with hydrothermal fluids that have flowed in contact with radiogenic rocks (Fig. 11). From the data set, there is no clear relationship between a given fracture set and a particular isotopic signature of the cements. Hence, there is no obvious control of the fracture pattern on the fluid flow in the structure. However, the veins with the most depleted $\delta^{18}O$ values are related to set S-II, L-II but also S-III, suggesting periods of mobilization of basement-derived fluids, namely during the Sevier time, like at SMA in set S-III. This observation, along with the eastward migration of basement-derived fluids in cover rocks emphasized by the eastward decrease in radiogenic signatures (Fig. 11), suggests that basement-derived fluids may have flowed continuously from the West of the basin in Carboniferous and Permian strata during Sevier event, mixing with formational fluids and precipitating during vein opening. Alternatively, some basement-derived hydrothermal fluids could have flowed through set S-II joints (i.e. as in RMA) despite a limited fracture development in the easternmost part of the basin (Amrouch *et al.*, 2010; Beaudoin *et al.*, 2012). We can also consider that some set S-III joints were reopened during the syn-folding stage because their orientation is nearly similar to that of L-II joints, as also suggested for SMA (Beaudoin *et al.*, 2011). This alternative interpretation can, however, only be invoked near the hinge where curvature is high.

At BHM, considering $\delta^{18}O$ values of vein cements along with the relative isotopic equilibrium between veins and host-rocks (Fig. 10a, b) and considering that fractures developed at the same burial depth as at SMA and LSMA (about 2.8 km above the Madison Fm.; Rioux, 1994), the palaeofluid system consists of formational fluids precipitated at thermal equilibrium with surrounding host-rocks, with no apparent mixing with basement-derived fluids. BHM being the biggest arch of the basin, such a closed fluid system may be related to (1) a bias in the sample distribution (the hinge is eroded, only the forelimb was sampled), (2) the early uplift of this structure (Crowley *et al.*, 2002), and/or (3) the easternmost location of this structure in the basin. In the latter case, BHM may have been located too far away from the source to be reached during the eastward migration of basement-derived fluids in the cover or in the basement (see below). Nevertheless, the closed fluid system in BHM remains consistent with the other described systems at fold-scale before events of pulses of basement-derived fluids (e.g. set S-I in RMA).

At PA, isotopic signatures of veins are in equilibrium with surrounding host-rocks (Fig. 10b); they also exhibit depleted carbon isotope values (Fig. 10a), which can be related to migration of hydrocarbons that are exploited, for example, within the BO (Stilwell *et al.*, 2010). Fluid inclusion microthermometry and timing of vein development reveal that fluids are at a thermal equilibrium with their surrounding environment, considering a 25 °C km^{-1} geothermal gradient (Brigaud *et al.*, 1990). Thus, the fluid system in PA also reflects a closed system with formational fluids that precipitated at thermal and chemical equilibrium with host-rock (Fig. 14). In contrast to BHM, the isotopic equilibrium between veins and host-rocks (Fig. 10b) and the observation of the same luminescence between vein cement and carbonate portion of host-rocks suggest that the fluids are formational fluids mobilized in the local porosity of the surrounding host-rock, without any large-scale migration. Fig. 13 highlights that fluids precipitated in PA are slightly different from fluids that flowed in SMA and RMA, and this may be considered as a difference between Palaeozoic and Jurassic formational fluid signatures. The absence of a basement-derived pulse affecting this fold can be related to (1) the vertical distance between the basement thrust tip (which ends in Palaeozoic formations after Stone, 1987) and the sampled Jurassic formations (the pathway involving 300 m of impermeable shales of the Gypsum Spring), and/or (2) the morphology of PA, which exhibits a more distributed hinge than other studied basement cored folds, implying a more scattered curvature-related joint network, or (3) the morphology of PA that may suggest that this fold is not basement-cored, although it is suggested by subsurface data (Stone, 2003).

As a result, fluid systems reconstructed in individual folds of the BHB depict a common evolution of fluid history at the basin scale. Along with local specific conditions at fold-scale, the evolution of fluid systems in folds consequently provides constraints on fluid migration timing, pathways and advection processes within the basin. This fluid history involves alternation of a fluid system dominated by formational fluids (local and basinal) and of

another fluid system dominated by basement-derived hydrothermal fluids (likely of meteoric origin). The limited mixing and diffusion processes happening during pulses of hydrothermal basement-derived fluids in the cover suggest fast migration and precipitation of these fluids at these times. Noticeably, the periods of basement-derived fluid pulses are correlated with timing of opening of extension-related fractures, related either to large-scale foreland flexure or to local-scale strata curvature at fold hinges above basement thrusts. Based on low values of salinity, isotopic signatures and highly radiogenic signatures (Figs. 10, 11, 12 and 13), it is proposed that these basement-derived fluids have a meteoric origin and have subsequently flowed first down into the basement and then upwards probably as early as during Cretaceous and not only during the Palaeocene, as first proposed at SMA (Beaudoin *et al.*, 2011).

Fluid migration pathways at basin scale: structural implications

Geochemical data show that basement-derived (radiogenic, hydrothermal and with meteoric origin) fluids have precipitated in the BHB. The interpretation of geochemical signatures of these basement-derived fluids with respect to the timing of microstructure development highlights that this precipitation occurred earlier in the western part of BHB, located close to the orogenic front, than in the eastern part. In the easternmost part of the basin, basement-derived fluids dominated the fluid system later in the basin history, mainly during strata folding. This difference in timing is related to the occurrence of set S-II (flexure-related) extensional fractures, probably formed during the early Sevier event, which are more represented in the western part of the BHB than in the eastern one (Beaudoin *et al.*, 2012), because of (1) difference in mechanical stratigraphy across the basin (Barbier *et al.*, 2012b) and/or (2) the western location of the flexural forebulge and related extension (Decelles, 2004). According to the palinspastic reconstructions of Decelles (2004), the location of the flexural forebulge during the Turonian is consistent with the position of RMA and the meteoric fluids could have flowed down into the basement during the Sevier orogeny through thrusts of the Idaho-Montana Sevier thrust belt since early Cretaceous (Figs 15a-1 and 16a) (e.g. Bebout *et al.*, 2001; Fig. 1d). Such an infiltration of meteoric fluids down to the basement rocks has already been suggested in other Sevier and Laramide flexural basins and in other parts of the orogens (Budai & Wiltschko, 1989; Nesbitt & Muehlenbachs, 1995; Bebout *et al.*, 2001; Fitz-Diaz *et al.*, 2011), where the isotopic signature of the fluids implies that meteoric fluids have flowed down to a depth of 10 km, reaching $\delta^{18}O$ values about $-15‰$ SMOW (e.g. Nesbitt & Muehlenbachs, 1995). This is consistent with our interpretation of basement-derived fluids, constituted of meteoric water, subsequently diluted by basinal fluids.

In such a case, fluids may have flowed *per descensum* along surficial joints in the sedimentary cover (Fig. 14b-1; e.g. in Fitz-Diaz *et al.*, 2011), then in damaged zones of faults, according to the fault-valve model (Sibson, 1981; Henderson & McCAIG, 1996) that considers that the post-seismic phase is associated with a decrease in fluid pressure at depth, allowing faults to pump fluids down (Fig. 15b-1). Below the basement top, fluids may have flowed (1) in the numerous fractures in the basement and/or (2) along the basement thrusts located in the inner part of the orogen (Decelles & Coogan, 2006 (Fig. 15b-1), even though the Sevier belt is thin-skinned in its frontal part.

Considering that meteoric fluids infiltrated the basement rocks in the inner part of the Sevier orogen, located about 200 km westwards from the actual front of the Sevier thrust belt (Decelles & Coogan, 2006), the proposed circulation model implies an eastward fluid migration in the basement over horizontal distances of 300 km (Figs 15 and 16). After the pulse related to the Sevier foreland flexure, an eastward migration in the cover rocks of about 80 km (distance between RMA and SMA, Fig. 15b) is exhibited by the difference in radiogenic ratios of fluids precipitated in the western part and eastern part of the basin (Fig. 11). Considering the pulse of hydrothermal basement-derived fluids documented during folding at SMA (Beaudoin *et al.*, 2011), a similar eastward migration of hydrothermal fluids probably occurred in the basement rocks (Fig. 15). This interpretation is consistent with previous works that evidenced long-range brine migrations during Sevier-Laramide times across North America (Bethke & Marshak, 1990).

Considering the timing of infiltration of meteoric fluids (during early Cretaceous), the timing of the pulse of basement-derived fluids through the flexural forebulge (during Turonian), and the time between this pulse and the precipitation in set L-I of diluted basement-derived fluids in the eastern part of the basin (considering Campanian time as the beginning of Laramide contraction), the time lapse during which fluids migrated laterally over 300 km ranges between 25 and 50 Myr (considering beginning of migration from the Sevier thrust belt since early Cretaceous or just before Turonian, respectively). Thus, this approach provides a rough estimate of the rate of basement-derived fluid migration at foreland-scale, ranging from 6 to 12 km Myr^{-1} in the basement rocks. It is also possible to approach the rate of the basin-scale eastward migration of basement-derived fluids in the cover by considering the time of their expulsion at RMA (Turonian) until they flow in sets L-I and L-II at SMA 80 km East of RMA (not before Campanian; Decelles, 2004). This leads to a flow rate about 8 km Myr^{-1} in the cover rocks. These rates, in either basement or cover rocks, are consistent with rates of migration of fluids in other forelands, such as in Venezuela (5–20 km Myr^{-1}; Schneider, 2003). In spite of studies that document fluid migration in fractured granites (Boiron *et al.*, 2002; Fourcade *et al.*, 2002) and along porosity developed in feldspath cracks (Géraud

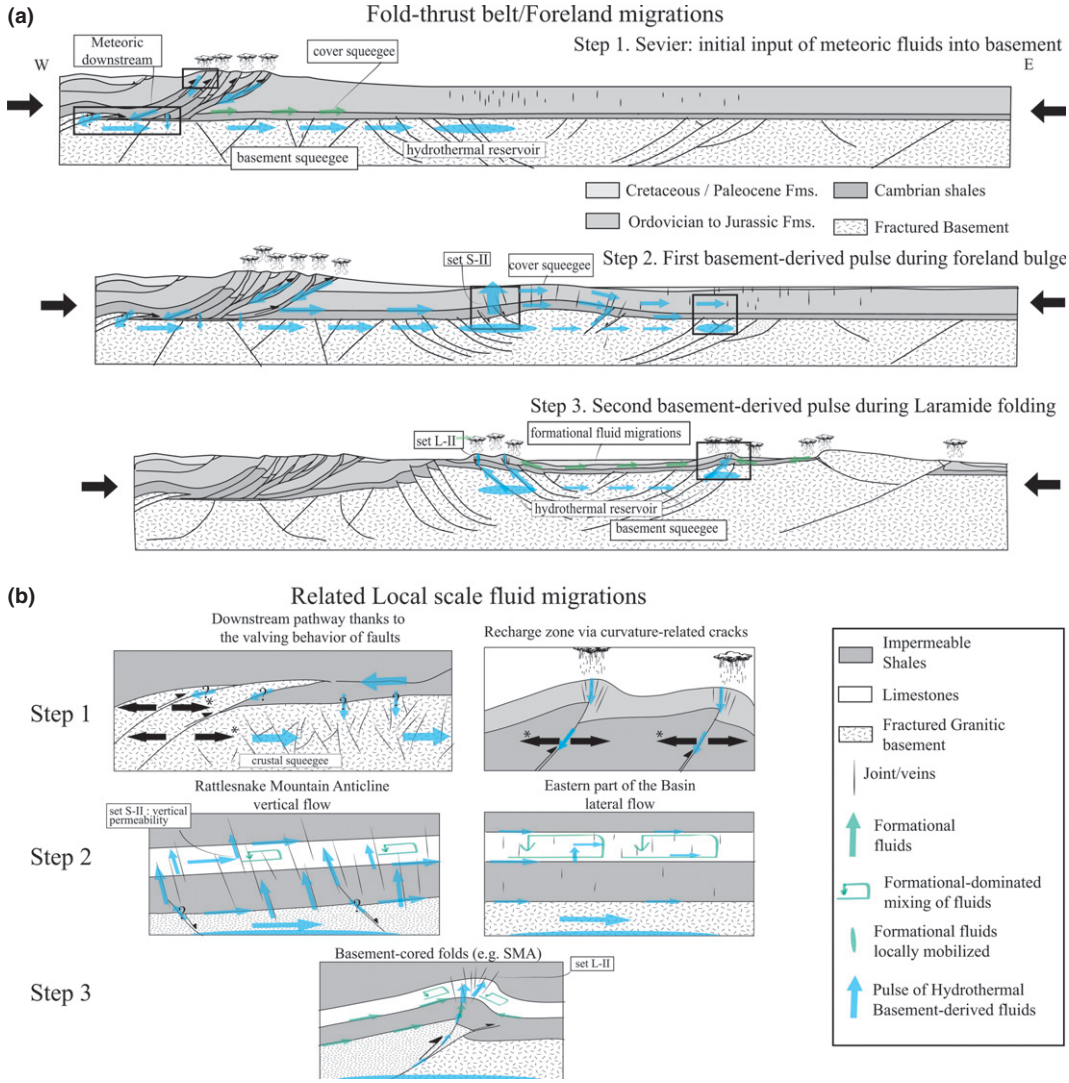

Fig. 15. (a) Conceptual model of the basin scale palaeohydrology evolution reported on a schematic E–Wcross-section (not to scale). 38 Geology is reported using grey- colour scale; light blue and green symbols represent palaeofluid system (arrows: migration, ellipsoids: reservoirs, blue for basement-derived fluids, green for formational fluids). The western Sevier Wyoming-Idaho thrust belt is used as migration pathway of meteoric fluids from surface down into basement rocks during Sevier time (step 1). This is followed by a crustal-scale lateral migration of those fluids, remobilized in the cover using the syn-flexure fractures (Sevier, step 2) and later, thanks to the syn-folding fractures and to the reactivated basement thrust (Laramide, step 3). (b) Zooms for each step show important features like downstream migration pathways (step 1), pathways marked with asterisk (*) are viable only during the syn- and post-seismic phase (see text for details) and fold-scale fluid evolution (steps 2 and 3). Arrows of fluid migration through the basement are schematic (b, step 1): the flow most likely followed connected basement fractures; the pathways were not linear although represented linear for simplicity.

et al., 2003), basement rocks are usually not considered as a very permeable medium, thus, the slowest inferred migration velocity is the more likely.

The driving force for such a large-scale fluid migration in basement rocks may result from various processes. Considering the permeability of rocks, Ge & Garven (1989) showed that the range migration velocity of fluids in a squeegee-type flow should be between 1 and 10 km Myr^{-1}. Because such process can expel fluids at rates up to 100 km Myr^{-1} but over short time span only (Bachu, 1995), squeegee-type fluid flow is unlikely to be the only driving mechanism. The most efficient driving forces for large-scale fluid migrations could be fluid thermal gradients coupled to lateral variations of topography (Lyubetskaya & Ague, 2009). Thus, in the western part of the thrust-belt during Sevier times, a likely hypothesis is that first, a squeegee-type lateral fluid flow occured and second, thermal and topographic lateral variations due to flexure drove fluids eastwards in basement rocks. The lateral migration of fluids in the basement can also be enhanced by the low-permeability seal make up by the nonpermeable Cambrian shales of the Gros Ventre formation. The invoked squeegee-type fluid flow (after Oliver, 1986) is consistent with progressive stress build-up within the Sevier-Laramide foreland as well as eastward thrust propagation (see part 4.1 and Beaudoin *et al.*,

2012). Such a long-distance, tectonically controlled fluid migration has been documented in other parts of the Rocky Mountains thrust belt, either in the cover rocks along lithological interfaces or/and porosity in limestone or sandstone formations (Bethke & Marshak, 1990; Qing & Mountjoy, 1992; Ulmer-Scholle & Scholle, 1994; Machel & Buschkuehle, 2008; Fitz-Diaz *et al.*, 2011; Barbier *et al.*, 2012b) or/and in the form of pulses of hydrothermal basement-derived fluids (so-called "hot flash", Machel & Cavel, 1999).

We propose that several events of basement-derived fluid circulation are characterized by pulses of heated meteoric fluids (i.e. 'hot-flash'-type vertical migrations). Thus, during the Sevier orogeny, meteoric fluids should have migrated laterally in the highly fractured and radiogenic basement rocks due to tectonic compression and topography formed by the forebulge, causing a migration at the upper crust scale (Figs 15a-1 and 16). Once fluids reached the western portion of the basin, they were vertically expelled off the

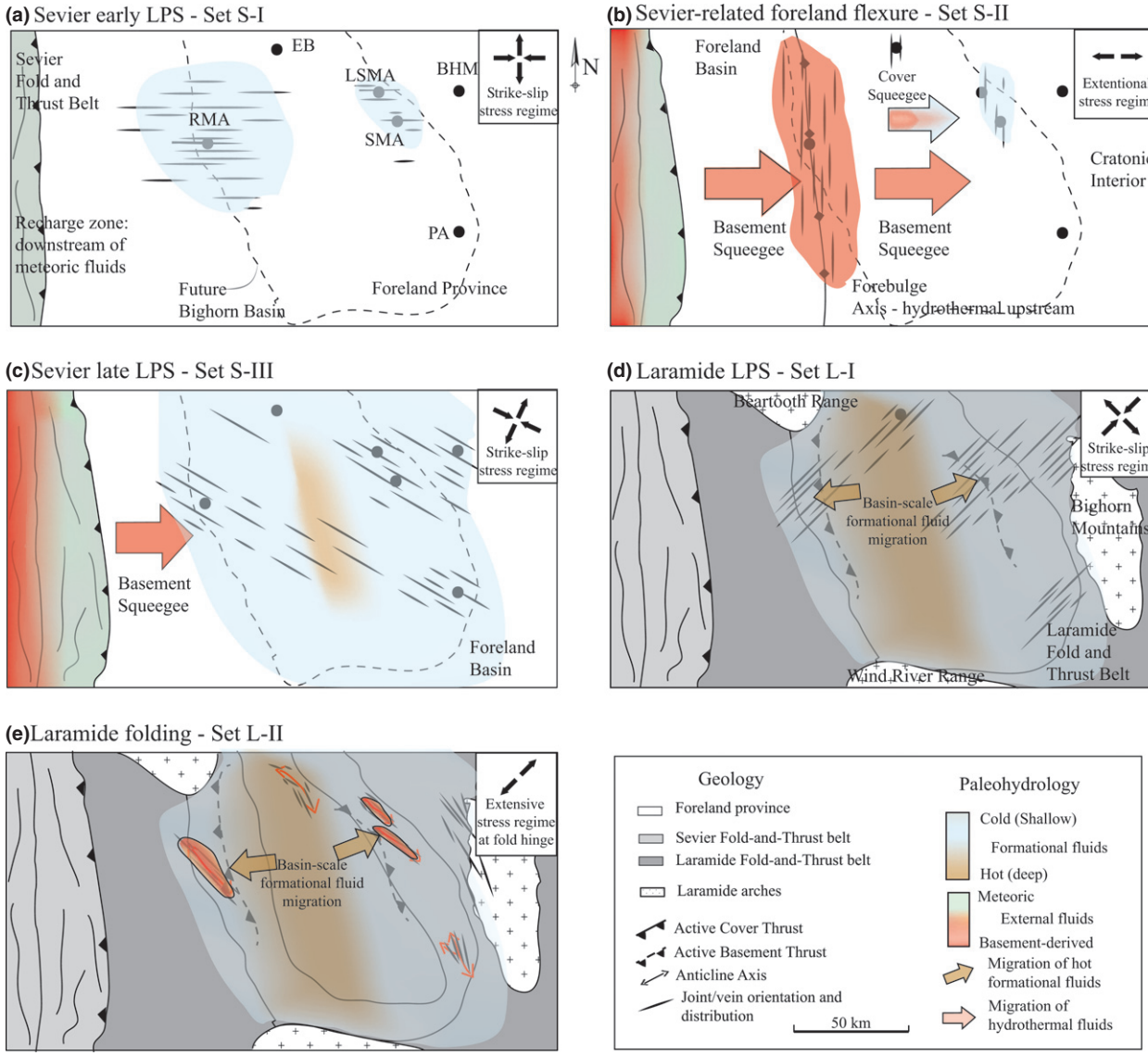

Fig. 16. Map-view synthesis of fracture development and associated fluid migrations in the Sevier fold-thrust belt and foreland (a, b, c) and in the Laramide fold-thrust belt (d, e). The maps represent palaeo-provinces of the orogeny and forebulge location according to palinspastic reconstructions of Decelles (2004), light grey being the Sevier Fold-thrust belt, white the foreland domain and dark grey the Laramide fold-thrust belt. Basement-derived hydrothermal fluids are represented according to temperature by the colour scale from red-to-green (according to d18O depletion and Th value) and formational fluids are represented according to temperature by the colour scale from orange-to-blue. Red arrows symbolize crustal-scale squeegee in the basement and red-to-blue arrow symbolizes the related dilution of the basement-derived fluids in the cover rocks. Orange arrows are related to the migration of the hot formational fluids from the deeper parts of the basin to the shallow edges. Horizontal scale between the Sevier fold-thrust belt front and the fold location is exaggerated. Distance between Rattlesnake Mountain Anticline and Sheep Mountain Anticline is 80 km.

basement (Figs 15a-2 and 16b) during foreland flexure and related extension. The possible reactivation of pre-existing basement faults (Marshak *et al.*, 2000) as normal faults due to foreland flexure (Fig 15b-2, e.g. Yu & Chou, 2001) could have enabled basement-derived fluids to flow upwards from the basement. In the cover, this upward fluid flow was fast in spite of 1 km-thick nonpermeable shales that overlie the basement. Thus, it most likely occurred in the cover within the syn-flexure fractures (i.e. set S-II joints, Fig. 15b) used as preferential drains, suggesting that they efficiently enhanced the vertical hydraulic permeability of strata. The next step in our scenario is the eastward flow of basement-derived radiogenic fluids across less radiogenic material (Fig. 16b, c), along with dilution by poorly radiogenic fluids (local formational fluids) (Fig. 11). Such a lateral migration at the basin scale presumably used lithological interfaces or/and porosity in limestone or sandstone formations (Fig. 15a), respectively the Bighorn/Madison/Phosphoria and Flathead formations, as proposed by several authors (Bell, 1970; Ulmer-Scholle & Scholle, 1994; Barbier *et al.*, 2012b). During the formation of set S-III and L-I, the lack of basement-derived fluid pulse suggests that the hydraulic permeability of the cover rocks was low, the fluid system being dominated by formational fluids (Figs. 16c, d). The highest temperature of entrapment recorded at SMA (Th = 140 °C, Beaudoin *et al.*, 2011) along with the highly depleted $\delta^{18}O$ signatures recorded in set L-II calcite in the same fold can only be explained by a later basement-derived upward fluid migration from basement to cover rocks (Figs 15a-3 and 16c, d). This highlights (1) the existence of a reservoir of basement-derived hydrothermal fluids underneath the eastern part of the basin, implying an eastward fluid migration at the basin scale in the basement rocks and (2) a late control of both basement thrusts and syn-folding fractures on the upward flow of basement-derived fluids. Such a late fluid flow event could not be documented at RMA because of outcrop conditions, but remains likely considering the similar kinematic evolution of both folds (Beaudoin *et al.*, 2012). The closed fluid system at BHM also implies that there were no basement-derived fluids in this easternmost part of the fold, suggesting that the eastward migration of fluids in the fractured basement rocks did not reach this part of the foreland.

To explain the highly radiogenic signatures of fluids in the western part of the basin, an alternative to the model of fluid migration in the basement rocks would be to consider a fluid migration at depth in porous K-feldspar rich sandstones, such as those of the lower Cambrian Flathead arkosic Formation. Although it is possible that fluids have flowed in the lower parts of the Flathead sandstones instead of deeper in the basement rocks, this formation is thin (<30 m) and discontinuous at the scale of the BHB (Thomas, 1965), which implies that fluids migrated also in basement rocks, at least locally where the arkosic Flathead Formation is absent. Another possible hypothesis to explain the highly radiogenic signatures of hydrothermal fluids would be to consider another fluid source such as the radiogenic fluids generated from Precambrian sedimentary basins in western Montana and Idaho (the Precambrian Belt Basins, Harrison, 1972) during Sevier fold and thrust belt development. This would be consistent regarding the strontium isotopic ratios (from 0.7048 to 0.7499, Hall & Veizer, 1996). Nevertheless, these fluids were saline and oxygen isotopic signatures of these Precambrian fluids are notably different from the $\delta^{18}O$ of vein cements in the BHB (21‰ SMOW against −10‰ SMOW, respectively; Koch *et al.*, 1995; Hall & Veizer, 1996), that are so more consistent with heated meteoric fluids.

Moreover, our data set contradicts previous interpretations of a relationship between the minimal depth of migration of hydrothermal fluids in folds and the amount of throw along Laramide basement thrusts (Katz *et al.*, 2006). Indeed, although the most radiogenic fluids are identified at RMA, where the basement thrust throw is larger than at SMA/LSMA (Erslev, 1995; Stanton & Erslev, 2004; Neely & Erslev, 2009; Beaudoin *et al.*, 2012), the fluids resulting in the most depleted (in terms of stable oxygen isotopes) and radiogenic calcites were recognized in pre-Laramide veins (Set S-II). This suggests that hydrothermal fluids were involved in the system during the Sevier flexural foreland evolution that predates the activation of Laramide basement thrusts (Figs. 15a-2). Our model also differs from the fluid flow model proposed by Barbier *et al.* (2012b) based on the study of the sole Madison Formation at only two localities, SMA and RMA. Their model explains geochemical data recorded at SMA by a lateral migration of formational fluids (locally mixed with meteoric fluids) from the deepest western parts of the basin to the eastern edge through secondary porosity (such as fractures) of the Madison and underlying formations. However, this model does not explain fluid inclusions and Sr isotopic data newly collected at RMA as well as the additional (O, C) isotopic analyses in veins from numerous other folds in the BHB, which show that the same fluid system existed in the sedimentary formations above and below the Madison Formation. The radiogenic values of the fluids that flowed in RMA fractures can only be explained by invoking pulses of fluids flowing in contact with basement (or basement-derived) rocks in the western part of the BHB as already proposed by Beaudoin *et al.* (2011) in its eastern part. This emphasizes the need for a complete spatial and stratigraphic sampling to reliably decipher the palaeohydrogeological history at the basin scale.

During folding, in basement-cored folds, the fluid system is opened to basement-derived fluids that previously flowed in the basement rocks, the thrusts acting as drains in the nonpermeable cover until fluids reach fractured formations (Beaudoin *et al.*, 2011). This is in con-

trast to numerous studies of the fold-scale fluid system in detachment folds (Lefticariu *et al.*, 2005; Travé *et al.*, 2007; Fischer *et al.*, 2009; Dewever *et al.*, 2011; Evans *et al.*, 2012) where the fluid system is stratified until the development of syn-folding fracture sets, which allow an upward flow of fluids from deeper formations in fractures (joints and faults). Thus, fluids involved in detachment folds are mainly formational fluids, mobilized at different depths during deformation, this depth being limited by the vertical persistence of fractures controlled by mechanical stratigraphy. The difference in fluid system in basement-cored folds and detachment folds highlights that the fluid system during folding seems to be partially controlled by the tectonic style, thick-skinned deformations allowing hydrothermal fluids to flow during folding, from the basement through the fractured cover rocks.

Our results finally reveal that fracture sets have different vertical drain capabilities, from zero (e.g. in PA, or set S-III at RMA) to very efficient; in the latter case, they allowed an upward migration of basement-derived fluids (in sets S-II and P-I of RMA and set L-II of SMA) through the impermeable shaly Gros Ventre formation at a rate which prevented significant mixing with local fluids or diffusion processes with host-rocks during migration and precipitation. This interpretation supports a control of the stress regime on the hydraulic permeability of fractures, as proposed by Sibson (1994). Accordingly, using the timing of pulses of basement-derived hydrothermal fluids, we therefore suggest that the more efficient fractures for vertical fluid migration are those that developed under extensional stress regime (Fig. 17a) rather than in LPS-related strike-slip stress regime (Fig. 17b).

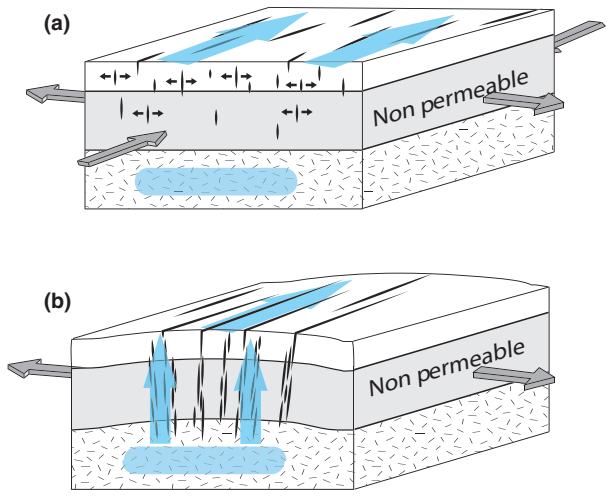

Fig. 17. Sketch showing hydraulic permeability of fracture according to the controlling stress regime. (a) Fractures developed under strike-slip stress regime are bad vertical drains. (b) Joints developed under extensional stress regime are good vertical drains.

CONCLUSIONS

This contribution reports an integrated study of fracture populations and related palaeohydrological system at the scale of the BHB, within the Palaeozoic succession. Since the formation of this basin as flexural foreland during the thin-skinned Sevier orogenic phase, the prevailing fluid system includes a mix at different degrees between formational fluids (from local host-rocks or from other parts of the basin) and basement-derived hydrothermal fluids composed of Cretaceous meteoric fluids that flowed downwards and were heated up in the basement. Three pulses of upward basement-derived hydrothermal fluids are documented in the basin at specific stages of the tectonic history: during the foreland flexure, during the Laramide folding event and during the post-Laramide extension event. These tectonically induced pulses are related to fracture/fault development and were consequently documented only in the parts of the foreland basin that were uplifted by later Laramide folding and subsequently partly eroded. Between pulses, formational fluids, mixed locally with remobilized basement-derived fluids, dominated the fluid system. Our results suggest an eastward, upper crustal-scale fluid migration event in both the cover and the basement during the Sevier contraction. Although geochemical data cannot discriminate among the driving forces for fluid migration, fluids are probably driven both by tectonic loading and by thermal and hydraulic gradients. The inferred lateral fluid migration rate ranging from of 6 to 12 km Myr^{-1} over 300 km is in accordance with previously published works.

Beyond regional implications, we emphasize that, within the sedimentary cover, the fluid system is stratified until extensional fractures developed efficient vertical drains. Our results further suggest that, among the numerous diffuse fracture sets observed in orogenic forelands, those developed under extensional stress regime (local strata curvature at fold hinge or regional-scale flexure) are probably the most efficient vertical migration pathways for fluid throughout the sedimentary cover.

ACKNOWLEDGEMENTS

This work was funded by Institut des Sciences de la Terre de Paris (ISTeP, UPMC, France). Authors thank R. Swennen, D. Deming, K. Bjorlykke, H. Machel and J. Nunn for their high-quality reviews that have greatly improved the original manuscript. The authors also thank G. Hurley and the Bureau of Land Management (BLM) of Cody, Wyoming, M.-C. Caumont at CREGU, the team of the CAI de Geochronologia (UCM) and Ph. Blanc from Lithologie Bourgogne for providing high-quality wafers. The authors also acknowledge N. Labourdette for high-quality measurements of stable isotopes of oxygen and carbon; the contributions of A. Boutoux and

stimulating discussions with J. Thibieroz, A. Verlaguet, J.-P. Callot and F. Roure.

SUPPORTING INFORMATION

Additional Supporting Information may be found in the online version of this article:

Table S1. Stable isotope (O, C, Sr) data set.

REFERENCES

Ahmadhadi, F., Daniel, J.-M., Azzizadeh, M. & Lacombe, O. (2008) Evidence for pre-folding vein development in the Oligo-Miocene Asmari Formation in the Central Zagros Fold Belt, Iran. *Tectonics*, **27**, TC1016.

Amrouch, K., Lacombe, O., Bellahsen, N., Daniel, J.-M. & Callot, J.-P. (2010) Stress and strain patterns, kinematics and deformation mechanisms in a basement-cored anticline: Sheep Mountain Anticline, Wyoming. *Tectonics*, **29**, TC1005.

Amrouch, K., Beaudoin, N., Lacombe, O., Bellahsen, N. & Daniel, J.-M. (2011) Paleostress magnitudes in folded sedimentary rocks. *Geophys. Res. Lett.*, **38**, L17301.

Anderson, D.W. & Picard, M.D. (1974) Evolution of synorogenic clastic deposits in the intermontane Uinta Basin of Utah. *SEPM Spec. Publ.*, **22**, 167–189.

Andrews, D.A., Pierce, W.G. & Eargle, D.H. (1947) Geological map of the Bighorn Basin, Wyoming and Montana. United States Department of the Interior, Geological Survey, 1:100,000.

Bacchu, S. (1995) Synthesis and Model of Formation-Water Flow, Alberta Basin, Canada. *AAPG Bull.*, **79**, 1159–1178.

Barbier, M., Hamon, Y., Callot, J.-P., Floquet, M. & Daniel, J.-M. (2012a) Sedimentary and diagenetic controls on the multiscale fracturing pattern of a carbonate reservoir: the Madion Formation (Sheep Mountain, Wyoming, USA). *Mar. Petrol. Geol.*, **29**, 50–67.

Barbier, M., Leprêtre, R., Daniel, J.-M., Gasparrini, M., Callot, J.-P., Hamon, Y., Lacombe, O. & Floquet, M. (2012b) Impact of fracturing stratigraphy on paleo-hydrodynamics, the Madison Formation case study (Bighorn Basin, Wyoming, USA). *Tectonophysics*, **576–577**, 116–132.

Beaudoin, N., Bellahsen, N., Lacombe, O. & Emmanuel, L. (2011) Fracture-controlled paleohydrogeology in a basement-cored, fault-related fold: Sheep Mountain anticline (Wyoming, USA). *Geochem. Geophys. Geosyst.*, **12**, Q06011.

Beaudoin, N., Leprêtre, R., Bellahsen, N., Amrouch, K., Callot, J.-P., Emmanuel, L. & Daniel, J.-M. (2012) Structural and microstructural evolution of the Rattlesnake Mountain Anticline (Wyoming, USA): new insights into the Sevier and Laramide orogenic stress build-up in the Bighorn Basin. *Tectonophysics*, **576–577**, 20–45.

Bebout, G.E., Anastasio, D.J. & Holl, J.E. (2001) Synorogenic crustal fluid infiltration in the Idaho-Montana thrust belt. *Geophys. Res. Lett.*, **28**, 4295–4298.

Bell, L.H. (1970) Depositional history of the Cambrian Flathead Standstone, Park County, Wyoming. *Wyoming Geol. Assoc. Guidebook*, **22**, 115–131.

Bellahsen, N., Fiore, P. & Pollard, D. (2006a) The role of fractures in the structural interpretation of Sheep Mountain Anticline, Wyoming. *J. Struct. Geol.*, **28**, 850–867.

Bellahsen, N., Fiore, P.E. & Pollard, D.D. (2006b) From spatial variation of fracture patterns to fold kinematics: a geomechanical approach. *Geophys. Res. Lett.*, **33**, 1–4.

Bethke, C.M. & Marshak, S. (1990) Brine migrations across North America – the plate tectonics of groundwater. *Annu. Rev. Earth Planet. Sci.*, **18**, 287–315.

Billi, A. (2005) Attributes and influence on fluid flow of fractures in foreland carbonates of southern Italy. *J. Struct. Geol.*, **27**, 1630–1643.

Bjørlykke, K. (1993) Fluid flow in sedimentary basin. *Sed. Geol.*, **86**, 137–158.

Bjørlykke, K. (1994) Fluid flow processes and diagenesis in sedimentary basins. In: *Geofluid: Origin, Migration and Evolution of Fluids in Sedimentary Basins* (Ed. by J. Parnell) *Geol. Soc. London Spec. Publ.*, **78**, 127–140.

Bjørlykke, K. (1999a) Principal aspects of compaction and fluid flow in mudstones. In: *Mud and Mudstones: Physical and Fluid Flow Properties* (Ed. by A.C. Aplin, A.J. Fleet & J.H.S. Macquaker) *Geol. Soc. London Spec. Publ.*, **158**, 73–78.

Bjørlykke, K. (1999b) An overview of factors controlling rates of compaction, fluid generation and fluid flow in sedimentary basins. In: *Growth, Dissolutions and Pattern Formation in Geosystems* (Ed. by B. Jamtveit & P. Meakin), pp. 381–404. Kluwer Akademic Publishers, Norwell.

Bjørlykke, K. (2010) Subsurface water and fluid flow in sedimentary basins. In: *Petroleum Geoscience. From Sedimentary Environments to Rock Physics* (Ed. by K. Bjørlykke), pp. 259–279. Springer, Berlin.

Blackstone, D.L. Jr. (1990) Rocky Mountain foreland structure exemplified by the Owl Creek Mountains, Bridger Range and Casper Arch, central Wyoming. In: *41st Annual Field Conference Guidebook* (Ed. by R.W. Specht), pp. 155–166. Wyoming Geological Association, Cheyenne.

Boiron, M.C., Cathelineau, M., Banks, D.A., Buschaert, S., Fourcade, S., Coulibaly, Y., Michelot, J.L. & Boyce, A. (2002) Fluid transfers at a basement/cover interface Part II. Large-scale introduction of chlorine into the basement by Mesozoic basinal brines. *Chem. Geol.*, **192**, 121–140.

Bons, P.D., Elburg, M.A. & Gomez-Rivas, E. (2012) A review of the formation of tectonic veins and their microstructures. *J. Struct. Geol.*, **43**, 33–62.

Bottinga, Y. (1969) Calculated fractionation factors for carbon and hydrogen isotope exchange in the system calcite-carbon dioxide-graphite-methane-hydrogen-water vapor. *Geochim. Cosmochim. Acta*, **33**, 49–64.

Brigaud, F., Chapman, D.S. & le Douaran, S. (1990) Estimating thermal conductivity in sedimentary basins using lithologic data and geophysical well logs. *AAPG Bull.*, **74**, 1459–1477.

Brown, W.G. (1988) Deformational style of Laramide uplifts in the Wyoming foreland. In: *Interaction of the Rocky Mountain Foreland and the Cordilleran Thrust Belt* (Ed. by C.J. Schmidt & W.J. Perry Jr) *G.S.A. Memoir 171*, Boulder, 1–26.

Bruckschen, P., Oesmann, S. & Veizer, J. (1999) Isotope stratigraphy of the European Carboniferous: proxy signals for ocean chemistry, climate and tectonics. *Chem. Geol.*, **161**, 127–163.

Budai, J.M. & Wiltschko, D.V. (1989) Isotopic exchange during tectonic veining: example from Absaroka Sheet in Wyoming overthrust belt. *Am. Assoc. Petrol. Geol. Bull.*, **73**, 338.

Chung, H.M., Brand, S.W. & Grizzle, P.L. (1981) Carbon isotope geochemistry of Paleozoic oils from Big Horn Basin. *Geochim. Cosmochim. Acta*, **45**, 1803–1815.

Coplen, T.B. (2007) Calibration of the calcite-water oxygen-isotope geothermometer at Devils Hole, Nevada, a natural laboratory. *Geochim. Cosmochim. Acta*, **71**, 3948–3957.

Coplen, T.B., Kendall, C. & Hopple, J. (1983) Intercomparison of stable isotope reference samples. *Nature*, **302**, 236–238.

Crowley, P.D., Reiners, P.W., Reuter, J.M. & Kaye, G.D. (2002) Laramide exhumation of the Bighorn Mountains, Wyoming: an apatite (U-Th)/He thermochronology study. *Geology*, **30**, 27–30.

Darton, N.H. (1905) Geologic map of the Bighorn Mountains Wyoming. U.S. Geological Survey, 1:100,000.

Decelles, P.G. (1994) Late Cretaceous–Paleocene synorogenic sedimentation and kinematic history of the Sevier thrust belt, northeast Utah and southwest Wyoming. *Geol. Soc. Am. Bull.*, **106**, 32–56.

Decelles, P.G. (2004) Late Jurassic to Eocene evolution of the Cordilleran thrust belt and foreland basin system, western USA. *Am. J. Sci.*, **304**, 105–168.

Decelles, P.G. & Coogan, J.C. (2006) Regional structure and kinematic history of the Sevier fold-and-thrust belt, central Utah. *Geol. Soc. Am. Bull.*, **118**, 841–864.

Deming, D., Nunn, J. A. & Evans, D.G. (1990) Thermal effects of compaction-driven groundwater flow from overthrust belts. *J. Geophys. Res.*, **95**, 6669–6683.

Dettman, D.L. & Lohmann, K.C. (2000) Oxygen evidence for high-altitude snow in the Laramide Rocky Mountains of North America during the Late Cretaceous and Paleogene. *Geology*, **28**, 243–246.

Dewever, B., Swennen, R. & Breesch, L. (2011) Fluid flow compartmentalization in the Sicilian fold and thrust belt: Implications for the regional aqueous fluid flow and oil migration history. *Tectonophysics*, doi:10.1016/j.tecto.2011.08.009.

Dickson, J.A.D. (1966) Carbonate identification and genesis as revealed by staining. *J. Sed. Petrol.*, **36**, 491–505.

Dietrich, D., McKenzie, J.A. & Song, H. (1983) Origin of calcite in syntectonic veins as determined from carbon-isotope ratios. *Geology*, **11**, 547–551.

Dubessy, J., Lhomme, T., Boiron, M.C. & Rull, F. (2002) Determination of chlorinity in aqueous fluids using Raman spectroscopy of the stretching band of water at room temperature: application to fluid inclusions. *Appl. Spectrosc.*, **56**, 99–106.

Durdella, M.J. (2001) Mechanical modeling of fault-related folds: West Flank of the Bighorn Basin, Wyoming. M.S. Thesis, Purdue University, West Lafayette.

Emrich, K., Ehhalt, D.H. & Vogel, J.C. (1970) Carbon isotope fractionation during the precipitation of calcium carbonate. *Earth Planet. Sci. Lett.*, **8**, 363–371.

Engelder, T. (1984) The role of pore water circulation during the deformation of foreland fold and thrust belts. *J. Geophys. Res.*, **89**, 4319–4325.

Engelder, T. (1987) Joints and some fractures in rocks. In: *Fracture Mechanics of Rock* (Ed. by B. Atkinson), pp. 27–69. Academic Press, Waltham.

Engelder, T., Gross, M.R. & Pinkerton, P. (1997) Joint development in clastic rocks of the Elk Basin anticline, Montana-Wyoming. In: *Fractured Reservoirs: Characterization and Modeling, Rocky Mountain Association of Geologists 1997 Guidebook* (Ed. T. Hoak, A. Klawitter & P. Blomquist, pp. 1–18. Rocky Mountain Association of Geologists, Denver.

Erslev, E.A. (1995) Heterogeneous Laramide deformation in the Rattlesnake Mountain Anticline, Cody, Wyoming. *Field Trip.*, **7**, 141–150.

Erslev, E.A. & Koenig, N.V. (2009) Three-dimensional kinematics of Laramide, basement-involved Rocky Mountain deformation, USA: insights from minor faults and GIS-enhanced structure maps. *GSA Mem.*, **204**, 125–150.

Evans, M.A. (2010) Temporal and spatial changes in deformation conditions during the formation of the Central Appalachian fold-and-thrust belt: evidence from joints, vein mineral paragenesis, and fluid inclusions. In: *From Rofinia to Pangea: The Lithotectonic Record of The Appalachian Region* (Ed. by R.P. Tollo, M.J. Bartholomew, J.P. Hibbard & P.M. Karabinos) *Geol. Soc. Am. Mem.*, **206**, 477–552.

Evans, M.A. & Fischer, M.P. (2012) On the distribution of fluids in folds: a review of controlling factors and processes. *J. Struct. Geol.*, **44**, 2–24.

Evans, M.A., Bebout, G.E. & Brown, C.H. (2012) Changing fluid conditions during folding: an example from the central Appalachians. *Tectonophysics*, **576–577**, 99–115.

Fanshawe, J.R. (1971). Structural evolution of Big Horn basin. Symposium on Wyoming Tectonics and their economic significance, 35–42.

Ferket, H., Swennen, R., Ortuño, S. & Roure, F. (2003) Reconstruction of the fluid flow history during Laramide foreland fold and thrust belt development in eastern Mexico: cathodoluminescence and $\delta^{18}O$-$\delta^{13}C$ isotope trends of calcite-cemented fractures. *J. Geochem. Explor.*, **78–79**, 163–467.

Fiore Allwardt, P., Bellahsen, N. & Pollard, D.D. (2007) Curvature and fraturing based on global positioning system data collected at Sheep Mountain anticline, Wyoming. *Geosphere*, **3**, 408–421.

Fischer, M.P., Higuera-Díaz, I.C., Evans, M.A., Perry, E.C. & Lefticariu, L. (2009) Fracture-controlled paleohydrology in a map-scale detachment fold: Insights from the analysis of fluid inclusions in calcite and quartz veins. *J. Struct. Geol.*, **31**, 1490–1510.

Fitz-Diaz, E., Hudleston, P., Siebenaller, L., Kirschner, D., Camprubi, A., Tolson, G. & Pi Puig, T. (2011) Insights into fluid flow and water-rock interaction during deformation of carbonate sequences in the Mexican fold-thrust belt. *J. Struct. Geol.*, **33**, 1237–1253.

Forster, A. & Evans, J.P. (1991) Fluid flow in thrust faults and crystalline thrust sheets: results of combined field and modeling studies. *Geophys. Res. Lett.*, **18**, 979–982.

Forster, A., Irmen, A.P. & Vondra, C. (1996) Structural interpretation of Sheep Mountain Anticline, Bighorn Basin, Wyoming. *Wyoming Geol. Assoc. Guidebook*, **47**, 239–251.

Fourcade, S., Michelot, J.L., Buschaert, S., Cathelineau, M., Freiberger, R., Coulibaly, Y. & Aranyossy, J.F. (2002) Fluid transfers at the basement/cover interface Part I. Subsurface recycling of trace carbonate from granitoid basement rocks (France). *Chem. Geol.*, **192**, 99–119.

Fox, J.E. & Dolton, G.L. (1995) Bighorn Basin Province (034). In: *National Assessment of United States Oil and Gas Resources – Results, Methodology, and Supporting Data*. (Ed. by D.L. Gauther, G.L. Dolton, K.I. Takahashi & K.L. Varnes) *U.S. Geol. Surv. Digital Data Ser.*, **30**, 1–22.

Ge, S. & Garven, G. (1989) . In: *The Origin and Evolution of Sedimentary Basin and Their Energy and Mineral Resources* (Ed. by R.A. Prince), *Am. Geophys. Union*, **99**, 145–157.

van Geet, M., Swennen, R., Durmishi, C., Roure, F. & Muchez, P. (2002) Paragenesis of Cretaceous to Eocene carbonate reservoirs in the Ionian fold and thrust belt (Albania): relation between tectonism and fluid flow. *Sedimentology*, **49**, 697–718.

Géraud, Y., Surma, F. & Mazerolle, F. (2003) Porosity and fluid flow characterization of granite by capillary wetting using X-ray computed tomography. In: *Applications of X-ray Computed Tomography in Geosciences* (Ed. by F. Mees, R. Swennen, M. Van Geet & P. Jacobs) *Geol. Soc. London Spec. Publ.*, **215**, 95–105.

Hall, S.M. & Veizer, J. (1996) Geochemistry of Precambrian carbonates: VII. Belt Supergroup, Montana and Idaho, USA. *Geochim. Cosmochim. Acta*, **60**, 667–677.

Hanor, J.S. (1980) Dissolved methane in sedimentary brines: potential effect on the PVT properties of fluid inclusions. *Econ. Geol.*, **75**, 603–609.

Harrison, J.E. (1972) Precambrian Belt Basin of Northwestern United States: its geometry, sedimentation, and copper occurrences. *Geol. Soc. Am. Bull.*, **83**, 1215–1240.

Heasler, H.P. & Hinckley, B.S. (1985) Geothermal resources of the Bighorn Basin, Wyoming. *Wyoming Geol. Surv.*, **8**, 27.

Henderson, I.H.C. & McCaig, A.M. (1996) Fluid pressure and salinity variation in shear zone-related veins, central Pyrenees, France: implication for the fault-valve model. *Tectonophysics*, **262**, 321–348.

Hennier, J.H. (1984) *Structural Analysis of The Sheep Mountain Anticline*. Texas A&S University, Bighorn basin, Wyoming. 118 pp.

Hennier, J.H. & Spang, J.H. (1983) Mechanisms for deformation of sedimentary strata at Sheep mountain anticline, Bighorn basin, Wyoming. *Wyoming Geol. Assoc. Guidebook*, **34**, 96–111.

Hilgers, C. & Urai, J.L. (2002) Microstructural observations on natural syntectonic fibrous veins: implications for growth process. *Tectonophysics*, **352**, 257–274.

Hubbert, M.K. & Willis, D.G. (1957) Mechanics of hydraulic fracturing. *Trans. AIME*, **210**, 153–166.

Katz, D.A., Eberli, G.P., Swart, P.K. & Smith, L.B. (2006) Tectonic-hydrothermal brecciation associated with calcite precipitation and permeability destruction in Mississippian carbonate reservoirs. Montana and Wyoming. *AAPG Bull.*, **90**, 1803–1841.

Kim, S.-T. & O'neil, J.R. (1997) Equilibrium and nonequilibrium oxygen isotope effects in synthetic carbonates. *Geochim. Cosmochim. Acta*, **61**, 3461–3475.

Koch, P.L., Zachos, J.C. & Dettman, D.L. (1995) Stable isotope and paleoclimatology of the Paleogene Bighorn Basin (Wyoming, USA). *Palaeogeogr. Palaeoclimatol. Palaeoecol.*, **115**, 61–89.

Laubach, S.E., Olson, J. & Gross, M.R. (2009) Mechanical and fracture stratigraphy. *AAPG Bull.*, **93**, 1413–1427.

Lefticariu, L., Perry, E.C., Fischer, M.P. & Banner, J.L. (2005) Evolution of fluid compartmentalization in a detachment fold complex. *Geology*, **33**, 69–72.

Li, K., Cai, C., He, H., Jiang, L., Cai, L., Xiang, L., Huang, S. & Zhang, C. (2011) Origin of palaeo-waters in the Ordovician carbonates in Tahe oilfield, Tarim Basin: constraints from fluid inclusions and Sr, C and O isotopes. *Geofluids*, **11**, 71–86.

Lopez, D.A. (2000) Geologic map of the Bridger 30' x 60' quadrangle, Montana. U.S. Geological Survey, 1:100,000.

Love, J.D. & Christiansen, A.C. (1985) Geologic map of Wyoming. U.S. Geological Survey, 1:500,000.

Lyubetskaya, T. & Ague, J.J. (2009) Modeling the magnitudes and directions of regional metamorphic fluid flow in collisional orogens. *J. Petrol.*, **50**, 1505–1531.

Machel, H.G. & Buschkuehle, B.E. (2008) Diagenesis of the Devonian Southesk-Cairn Carbonate Complex, Alberta, Canada: marine cementation, burial dolomitization, thermochemical sulfate reduction, anhydritization, and squeegee fluid flow. *J. Sed. Res.*, **78**, 366–389.

Machel, H.G. & Cavel, P.A. (1999) Low-flux, tectonically-induced squeegee fluid flow (« hot flash ») into the Rocky Mountain Foreland Basin. *Bull. Can. Petrol. Geol.*, **47**, 510–533.

Machel, H.G. & Lonnee, J. (2002) Hydrothermal dolomite – a product of poor definition and imagination. *Sed. Geol.*, **152**, 163–171.

Marshak, S., Karlstrom, K. & Timmons, J.M. (2000) Inversion of Proterozoic extensional faults: an explanation for the pattern of Laramide and Ancestral Rockies intracratonic deformation, United States. *Geology*, **28**, 735–738.

McCabe, W.S. (1948) Elk basin, anticline, Park county, Wyoming, and Carbon county, Montana. *AAPG Bull.*, **32**, 52–67.

McCaig, A.M. (1988) Deep fluid circulation in fault zones. *Geology*, **16**, 865–960.

Morrill, C. & Koch, P.L. (2002) Elevation or alteration? Evaluation of isotopic constraints on paleoaltitudes surrounding the Eocene Green River Basin. *Geology*, **30**, 151–154.

Neely, T.G. & Erslev, E.A. (2009) The interplay of fold mechanisms and basement weaknesses at the transition between Laramide basement-involved arches, north-central Wyoming, USA. *J. Struct. Geol.*, **31**, 1012–1027.

Nesbitt, B.E. & Muehlenbachs, K. (1995) Geochemical studies of the origins and effects of synorogenic crustal fluids in the southern Omineca Belt of British Columbia, Canada. *GSA Bull.*, **107**, 1033–1050.

Norris, R.D., Jones, L.S., Corfield, R.M. & Cartlidge, J.E (1996) Skiing in the Eocene Uinta Mountains? Isotopic evidence in the Green River Formation for snow melt and large mountains. *Geology*, **24**, 403–406.

Oliver, J. (1986) Fluids expelled tectonically from orogenic belts: their role in hydrocarbon migration and other geologic phenomena. *Geology*, **14**, 99–102.

Orr, W.L. (1974) Changes in sulfur content and isotopic ratios of sulfur during petroleum maturation – study if Big Horn Basin Paleozoic oils. *AAPG Bull.*, **58**, 2295–2318.

Pierce, W.G. (1966) Geologic map of the Cody quadrangle, Park County, Wyoming. U.S. Geological Survey, Geologic Quadrangle Map GQ-542, 1:62,500.

Pierce, W.G. & Nelson, W.H. (1968) Geologic map of the Pat O'Hara Mountain Quadrangle, Park County, Wyoming. U.S. Geological Survey, Geologic Quadrangle Map GQ-0755, 1:62,500.

Qing, H. & Mountjoy, E. (1992) Larger-scale fluid flow in the Middle Devonian Presqu'ile barrier, Western Canada Sedimentary Basin. *Geology*, **20**, 903–906.

Ramsay, J.G. (1980) The crack-seal mechanism of rock deformation. *Nature*, **284**, 135–139.

Reynolds, S.J. & Lister, G.S. (1987) Structural aspect of fluid-rock interactions in detachment zones. *Geology*, **15**, 362–366.

Rhodes, M.K., Carroll, A.R., Pietras, J.T., Beard, B.L. & Johnson, C.M. (2002) Strontium isotope record of paleohydrology and continental weathering, Eocene Green River Formation, Wyoming. *Geology*, **30**, 167–170.

Rioux, R.L. (1994) Geologic map of the Sheep Mountain - Little Sheep Mountain Area, Big Horn County, Wyoming. U.S. Geological Survey, 1:48,000.

Rogers, C.P. Jr, Richards, P.W., Conant, L.C., Vine, J.D. & Notley, D.F. (1948) Geology of the worland - Hyattville area, Big Horn and Washakie counties, Wyoming. Oil and Gas investigations preliminary map, 84, 1:48,000.

Rosenbaum, J. & Sheppard, S.M.F. (1986) An isotopic study of siderites, dolomites and ankerites at high temperatures. *Geochim. Cosmochim. Acta*, **50**, 1147–1150.

Roure, F., Swennen, R., Schneider, F., Faure, J.L., Ferkand, H., Guilhaumou, N., Osadandz, K., Robion, P. & Vandeginste, V. (2005) Incidence and importance of tectonics and natural fluid migration on reservoir evolution in foreland fold-and-thrust belts. *Oil Gas Sci. Technol.*, **60**, 67–106.

Roure, F., Andriessen, P., Callot, J.-P., Ferket, H., Gonzalez, E., Guilhaumou, N., Hardebol, N., Lacombe, O., Malandain, J., Mougin, P., Muska, K., Ortuno, S., Sassi, W., Swennen, R. & Vilasi, N. (2010) The use of paleo-thermobarometers and coupled thermal, fluid flow and pore fluid pressure modelling for hydrocarbon and reservoir prediction in fold-and-thrust belts. In: *Hydrocarbons in Contractional Belts* (Ed by G. Goffey, J. Craig, T. Needham & R. Scott) *Geol. Soc. London Spec. Publ.*, **348**, 87–114.

Rubey, W.W. & Hubbert, M.K. (1959) Role of fluid pressure in mechanics of overthrust faulting. II. Overthrust belt in geosynclmal area of western Wyoming in light of fluid-pressure hypothesis. *Geol. Soc. Am. Bull.*, **70**, 167–205.

Savage, H.M. & Cooke, M.L. (2004) The effect of non-parallel thrust fault interaction on fold patterns. *J. Struct. Geol.*, **26**, 905–917.

Schneider, F. (2003) Basin Modeling in Complex Area: Examples from Eastern Venezuelan and Canadian Foothills. *Oil Gas Sci. Technol.*, **58**, 313–324.

Sibson, R.H. (1981) Fluid flow accompanying faulting: field evidence and models. In: *Earthquake Prediction: An International Review* (Ed. by D.W. Simpson & P.G. Richards) *Am. Geophys. Union Maurice Ewing Ser.*, **4**, 593–603.

Sibson, R.H. (1994) Crustal stress, faulting and fluid flow. In: *Geofluids: Origin, Migration and Evolution of Fluids in Sedimentary Basins* (Ed. by J. Parnell) *Geol. Soc. London Spec. Publ.*, **78**, 69–84.

Stanton, H.I. & Erslev, E.A. (2004) Sheep Mountain Anticline: backlimb tightening and sequential deformation in the Bighorn Basin, Wyoming. *Wyoming Geol. Assoc. Guidebook*, **53**, 75–87.

Stearns, D.W. (1978) Faulting and forced folding in the Rocky Montains foreland. In: *Laramide Folding Associated With Basement Block Faulting in The Western United States* (Ed. by V. Matthews) *Geol. Soc. Am. Mem.*, **151**, 1–37.

Stilwell, D.P., Davis-Lawrence, S.W. & Elser, A.M. (2010) Reasonable foreseeable development scenario for oil and gas Bighorn Basin planning area, Wyoming. Final Rapport of the United States Department of the Interior, Bureau of Land Management, 176 pp.

Stone, D.S. (1987). Northeast-Southwest structural transect: Rocky Mountain foreland, Wyoming (abs.). *AAPG Bull.*, **71**, 1015, 1:24,000.

Stone, D.S. (1993) Basement-involved thrust-generated folds as seismically imaged in the subsurface of the central Rocky Mountain foreland. In: *Laramide Basement Deformation in The Rocky Mountain of The Western United States* (Ed by C.J. Schmidt, R.B. Chase & E.A. Erslev) *Geol. Soc. Am. Spec. Pap.*, **280**, 271–318.

Stone, D.S. (2003) New interpretations of the Piney Creek thrust and associated Granite Ridge tear fault, northeastern Bighorn Mountain, Wyoming. *Rocky Mt. Geol.*, **38**, 205–235.

Stone, D.S. (2004) Rio thrusting, multi-stage migration and formation of vertically segregated Paleozoic oil pools at Torchlight Field on the Greybull Platform (Eastern Bighorn basin): implication for exploration. *Mt. Geol.*, **41**, 119–138.

Templeton, A.S., Sweeney, J. Jr, Manske, H., Tilghman, J.F., Calhoun, S.C., Voilich, A. & Chamberlain, C.P. (1995) Fluids and the Heart Mountain fault revisited. *Geology*, **23**, 929–932.

Thomas, L.E. (1965) Sedimentation and structural development of Bighorn Basin. *AAPG Bull.*, **49**, 1867–1877.

Travé, A., Calvet, F., Sans, M., Vergés, J. & Thirlwall, M. (2000) Fluid history related to the Alpine compression at the margin of the south-Pyrenean Foreland basin: the El Guix anticline. *Tectonophysics*, **321**, 73–102.

Travé, A., Labaume, P. & Vergés, J. (2007) Fluid Systems in Foreland Fold-and-Thrust Belts: An Overview from the Southern Pyrenees. In: *Thrust Belts and Foreland Basins* (Ed by O. Lacombe, J. Lavé, F. Roure & J. Vergès, pp. 93–117. Springer, Berlin.

Ulmer-Scholle, D.S. & Scholle, P.A. (1994) Replacement of evaporites within the Permian Park City Formation, Bighorn basin, Wyoming, U.S.A. *Sedimentology*, **41**, 1203–1222.

Vandeginste, V., Swennen, R., Allaeys, M., Ellam, R.M., Osadetz, K. & Roure, F. (2012) Challenge of structural diagenesis in foreland fold-and-thrust belts: a case study on paleofluid flow in the Canadian Rocky Mountains West of Calgary. *Mar. Petrol. Geol.*, **35**, 235–251.

Veizer, J., Ala, D., Azmy, K., Bruckschen, P., Buhl, D., Bruhn, F., Carden, G.A.F., Diener, A., Ebneth, S., Godderis, Y., Jasper, T., Korte, C., Pawellek, F., Podlaha, O.G. & Strauss, H. (1999) $^{87}Sr/^{86}Sr$ $\delta^{13}C$ and $\delta^{18}O$ evolution of Phanerozoic seawater. *Chem. Geol.*, **161**, 59–88.

Vilasi, N., Malandain, J., Barrier, L., Amrouch, K., Callot, J.-P., Guilhaumou, N., Lacombe, O., Muska, K., Roure, F. & Swennen, R. (2009) From outcrop and petrographic studies to basin-scale fluid flow modelling: the use of the Albanian natural laboratory for carbonate reservoir characterization. *Tectonophysics*, **474**, 367–392.

Weil, A.B. & Yonkee, W.A. (2012) Layer-parallel shortening across the Sevier fold-thrust belt and Laramide foreland of Wyoming: spatial and temporal evolution of a complex geodynamic system. *Earth Planet. Sci. Lett.*, **357–358**, 405–420.

Wiltschko, D.V., Lambert, G.R. & Lamb, W. (2009) Conditions during syntectonic vein formation in the footwall of the Absaroka Thrust Fault, Idaho-Wyoming-Utah fold and thrust belt. *J. Struct. Geol.*, **31**, 1039–1057.

Yu, H.-S. & Chou, Y.-W. (2001) Characteristics and development of the flexural forebulge and basal unconformity of Western Taiwan Foreland Basin. *Tectonophysics*, **333**, 277–291.

Zheng, Y.F. (1999) Oxygen isotope fractionation in carbonate and sulphate minerals. *J. Geochem.*, **33**, 109–126.

Manuscript received 21 June 2012; In revised form 26 April 2013; Manuscript accepted 14 May 2013.

